Article

Dynamics and Site Isolation: Keys to High Propane Dehydrogenation Performance of Silica-Supported PtGa Nanoparticles

P.-A. Payard, L. Rochlitz, K. Searles, L. Foppa, B. Leuthold, O. V. Safonova, A. Comas-Vives,* and C. Copéret*

Read Online

ACCESS | Metrics & More | Article Recommendations | Supporting Information

ABSTRACT: Nonoxidative dehydrogenation of light alkanes has seen a renewed interest in recent years. While PtGa systems appear among the most efficient catalyst for this reaction and are now implemented in production plants, the origin of the high catalytic performance in terms of activity, selectivity, and stability in PtGa-based catalysts is largely unknown. Here we use molecular modeling at the DFT level on three different models: (i) periodic surfaces, (ii) clusters using static calculations, and (iii) realistic size silica-supported nanoparticles (1 nm) using molecular dynamics and metadynamics. The combination of the models with experimental data (XAS, TEM) allowed the refinement of the structure of silica-supported PtGa nanoparticles synthesized via surface organometallic chemistry and provided a structure−activity relationship at the molecular level. Using this approach, the key interaction between Pt and Ga was evidenced and analyzed: the presence of Ga increases (i) the interaction between the oxide surface and the nanoparticles, which reduces sintering, (ii) the Pt site isolation, and (iii) the mobility of surface atoms which promotes the high activity, selectivity, and stability of this catalyst. Considering the complete system for modeling that includes the silica support as well as the dynamics of the PtGa nanoparticle is essential to understand the catalytic performances.

PtGa/SiO₂
Multiscale Modelling (AIMD vs static DFT) & Spectroscopic Characterization (XAS, TEM)

KEYWORDS: propane dehydrogenation, DFT calculations, Ab initio molecular dynamics, metadynamics, C−H activation
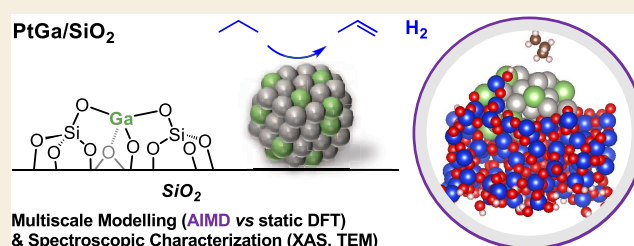
■ INTRODUCTION

Nonoxidative dehydrogenation of light alkanes is a key technology of the petrochemical industry that has seen a renewed interest in the recent years due to the increasing propene demand and to the simultaneous decommissioning of naphtha-crackers.[1] Indeed, the exploitation of shale gas has led to both a decrease production of propene by cracking and a surge of light alkanes such as propane (Figure 1, path a).[1] However, propane dehydrogenation (PDH) is challenging because the high endothermy of this reaction ($\Delta_r H$ = +124 kJ mol^{-1}) requires the use of high operation temperatures (above 500 °C), that favor both poor selectivity and rapid deactivation for both industrially used Cr- and Pt-based catalysts.[2−5] In that context, the overall PDH efficiency of Pt catalysts can be improved with metal additives/promoters that include transition (e.g., Cu,[6−9] Ir[10]) or p-block metals (e.g., Sn,[11−14] Ga,[15−25] In,[26−28] and Zn[29−33]). These additives allow an increase of both selectivity and lifetime of light alkane dehydrogenation catalysts,[2−5] while increased[7,8,10,11,17,33] or decreased[6] activity has been reported.

Large research efforts on the PtSn systems, one of the first commercial PDH catalysts (Olefex process), have demonstrated that these effects are partly related to the formation of a PtSn

alloy. The mechanism of PDH on PtSn alloys has been intensively studied both experimentally[34,35] and computationally.[34−41] PDH is proposed to take place through two consecutive oxidative additions of C−H bonds to Pt(0) while further dehydrogenation and C−C bond cleavage were proposed as a main pathway for coke formation (Figure 1).[38−40] Regarding catalyst stability, both coking (Figure 1, path c) and sintering of nanoparticles are proposed to explain deactivation. Experimentally, both reduced or increased coke-formation have been reported on PtSn compared to supported Pt,[14,42−46] while the addition of Sn also allows the reduction of sintering.[9b] On the basis of periodic DFT calculations,[41] the adjunction of Sn is proposed to minimize large Pt ensembles, thus disfavoring C−C cleavage (cracking, Figure 1, path b), and to decrease the affinity of the metal surface for propylene, thus limiting deep dehydrogenation.[6,43,46] While computational
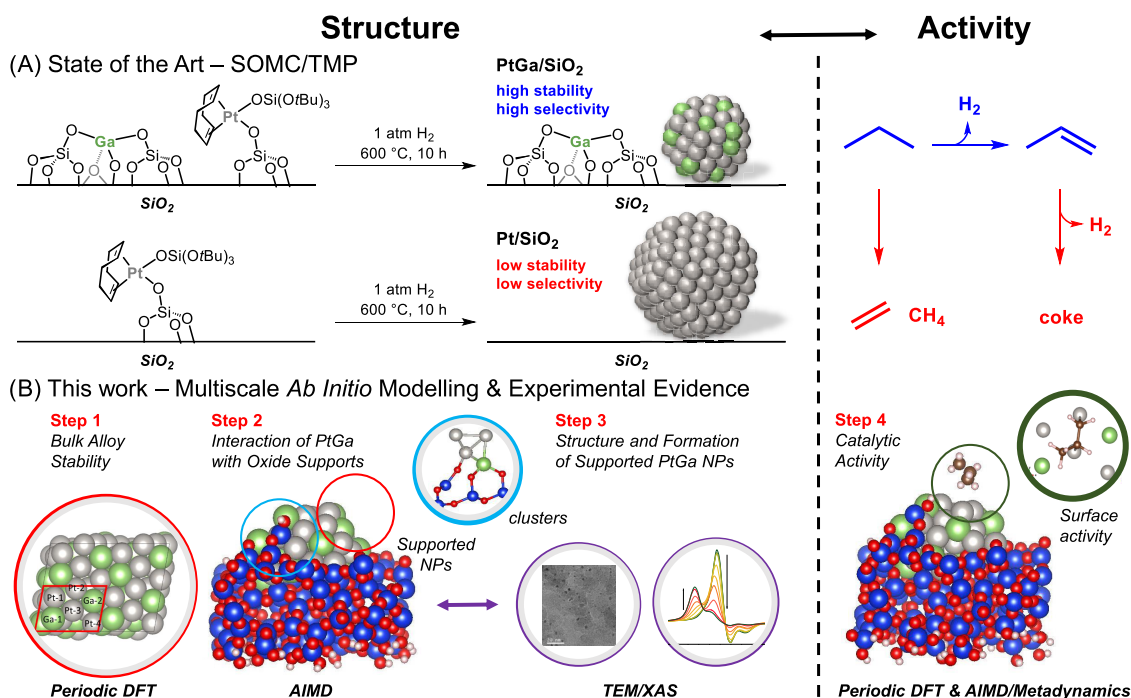
Figure 1. (A, Left) State of the art: PDH on PtGa system supported on silica, synthetic strategy using SOMC/TMP and proposed structure, see ref 6d. (Right) Products and byproducts. (B) General strategy of this paper: (1) structure of a Pt_2Ga (311) and (111) surfaces; (2) interphase, interaction of silica and Ga^{III} single-sites with Pt^0 and Ga^0; (3) structure of Pt and Pt_2Ga nanoparticles supported on oxides (SiO_2 and Ga-doped SiO_2); (4) activity of Pt_2Ga (311) and (111) surfaces compared to Pt (111) and comparison with activity of Pt and Pt_2Ga supported nanoparticles.

studies trying to tackle the effect of added Sn on the structure and stability of supported Pt nanoparticles are scarce, a joint XAS/molecular dynamic study on small supported PtSn clusters have evidenced the high mobility of the surface Pt/Sn atoms.[34,35] The high flexibility of such systems likely plays a role in the overall observed catalytic efficiency.

More recently, PtGa systems have also been implemented in production plants for propene production.[17,22,23,47] Despite major advances in this field, the nature of the active site for PDH in PtGa-based catalysts is not clear since Ga^{III} centers alone can also efficiently catalyze PDH in contrast to Sn^{IV}.[48−51] PDH on Ga^{III} sites is thought to take place through C−H activation leading to the formation of either Ga-hydride or Ga-alkyl species.[52−56] In PtGa systems, the dramatically increased performance compared to isolated Ga sites is sometime discussed in terms of a Pt-promotional effect, suggesting that the presence of Pt promotes the activity of Ga active sites.[17] In contrast to PtSn, the detailed understanding of the relation between the structure and the catalytic performance, as well as the role of Ga have not been proposed for these systems until now, neither experimentally nor via computational approaches.[57]

The difficulty in developing a molecular-level understanding of these systems partially arises from the lack of reported experimental data. PtGa materials are complex catalysts, making modeling and in-depth characterization as well as understanding of their reactivity very challenging. This complexity is often inherited from the synthetic method, which leads to a mixture of surface species. We recently prepared a silica-supported PtGa-catalyst for PDH ($PtGa/SiO_2$, Figure 1)[4,18] using surface organometallic chemistry (SOMC).[58−61] This synthetic approach allows for a more controlled introduction of each component (Ga and Pt) through sequential grafting and post-treatment steps.[59−62] Furthermore, this approach also facilitates

characterization as all of the potentially active phase is located on the support surface and can be selectively probed by spectroscopic techniques. In short, with SOMC, small and narrowly distributed $PtGa_x$ ($0.5 < x < 0.9$, size = ca. 1 nm) alloyed nanoparticles with a fraction of the Ga^{III} ($1 − x$) remaining as single-sites on the support surface were generated on silica (Figure 1). Such material displays outstanding productivity, selectivity, and stability in PDH[18] compared to a Ga^{III} single-site material prepared via the same approach[51] and conventionally synthesized PtGa systems. However, the exact nature of the surface sites, the mechanism of the nanoparticle formation from single sites and the origin of the reactivity of this model system remain to be understood at the molecular level. For instance, the exact location of Ga within the nanoparticle could not be fully resolved: no Ga−Ga neighbors could be detected within this PtGa alloy nanoparticles by extended X-ray absorption fine structure (EXAFS) spectroscopy, while the number of Ga−O neighbors seemed too large with respect to the amount of Ga^0. Furthermore, besides an increase in selectivity and stability compared to Pt nanoparticles or Ga^{III}-single sites supported on silica, the activity of this material is ca. 2 orders of magnitude higher than that of Ga^{III}-single sites alone, raising questions about the nature of the active sites and the origin of the improved catalytic performances.

The recent advances in computational chemistry methods, allowing the study of large scale systems by quantum approaches—in combination with carefully designed experiments and state of the art characterization techniques—allow for greater understanding where experimental data alone cannot provide sufficient answers due to the complexity of the investigated systems. In the present work, we therefore use this approach to refine the structural characterization of this PtGa system and to develop a structure−activity relationship.

We aim at answering the following questions (Figure 1):

i. What determines the structure of the PtGa alloy, how is it formed and what is the nature of the interaction between the nanoparticle and the support?

ii. What is the role of Ga in driving the PDH performance of the PtGa system by comparison to pure Pt and Ga isolated sites?

iii. How do residual Ga^{III} sites remaining on silica affect the structure and the reactivity of the PtGa nanoparticles?

Initially, we examined the structure of a PtGa nanoparticle supported on Ga-doped silica by comparing possible PtGa bulk structures by means of periodic Density Functional Theory (DFT) calculations. However, this simple periodic model cannot help unravelling the role of the oxide support as well as the cluster/nanoparticle size effects that experimentally proved to strongly impact the shape and reactivity of these systems.[63,64] Next, we thus investigated the role of the interface on the structure of supported 1 nm Pt and PtGa nanoparticles on model silica and Ga-doped silica surfaces by using *ab initio* molecular dynamics (AIMD)[65,66] at high temperature (875 K) to allow a more extensive exploration of the relevant configurational space and to refine the structure of the supported nanoparticles by integrating X-ray absorption spectroscopy (XAS) data. The PDH mechanism on the supported NPs was then evaluated using metadynamics simulations,[67–70] in order to rationalize the high performance and stability of the PtGa system compared to the Pt one. The results from metadynamics were contrasted with static calculations on crystalline surfaces to get more insight into the different operating effects and to identify the factors that dominate the catalytic properties of the system.

2. COMPUTATIONAL SECTION

Optimization of Bulk and Surfaces of Pt_2Ga

The Vienna ab initio Simulation Package (VASP) code[71–74] was used to optimize Pt_2Ga bulks and surfaces described in the first section of this paper. The PBE[75–78] functional in combination with plane-wave basis-set with pseudopotentials (PAW method)[79,80] with a cutoff energy of 400 eV was selected to calculate bulk properties of the metallic systems. The bulk was relaxed with a convergence criterion of 0.01 eV Å^{-1} and a 12 12 12 Monkhorst−Pack grid was used to sample the Brillouin-zone with a first-order Methfessel−Paxton smearing of 0.2 eV.

In principle, one can treat the metal component with the lowest abundance as an impurity in the lattice of the metal with the higher abundance. This is carried out by substituting platinum atoms of the bulk by the corresponding element and then evaluating the geometry of the obtained unit cell. To construct the alloy material a $3 \times 1 \times 1$ supercell of the platinum fcc unit cell was taken and four Pt atoms were exchanged by Ga, obtaining a Pt/Ga ratio equal to 2:1.

Surfaces were constructed by cleavage of the most stable bulk structure following the lattice planes using six rows of atoms and a vacuum spacing in the direction perpendicular to the surface (14 Å). Each surface was optimized at the same level of theory used for bulk (see above), and the uppermost three layers of the metallic surface were relaxed with a convergence criterion of 0.01 Å^{-1}; the other layers were kept fixed in the bulk geometry.

The silica-supported PtGa nanoparticles that show high catalytic performance in PDH have a Pt/Ga stoichiometry comprised between 1:1 and a 2:1.[6d] To obtain a first evaluation of the factors governing the stability of Pt_2Ga alloys, 14 different bulk structures ([Figure S1] for structure and [Table S1] for energy)

with the stoichiometry Pt_2Ga were generated by exchanging Pt with Ga atom(s) starting from face centered cubic (fcc) Pt (see this section).

Reactivity of the Pt_2Ga

The Vienna ab initio Simulation Package (VASP) code[71–74] was also selected for the first parts of this work, the opt-PBE[75–78] functional—including van der Waals corrections (opt-PBE-vdW)—in combination with a plane-wave basis-set with pseudopotentials (PAW method)[79,80] with a cutoff energy of 400 eV was used. The use of van der Waals correction is required to estimate the interaction of propane with Pt and PtM surfaces.[81] Both Pt (111) (reference) and Pt_2Ga (111) surfaces were modeled by a supercell (9 Å × 7 Å × 26 Å and 15 Å × 11 Å × 26 Å, respectively) including six rows of atoms and vacuum spacing in the direction perpendicular to the surface (14 Å). A 2 2 1 Monkhorst−Pack grid was used to sample the Brillouin-zone together with a first-order Methfessel−Paxton smearing of 0.2 eV. A dipole correction was used for adsorbed molecules.[82] All the molecules and the uppermost three layers of the metallic surface were relaxed with a convergence criterion of 0.01 eV Å^{-1}; the other layers were kept fixed in the bulk geometry. This level of theory was demonstrated to be accurate for estimation of adsorption energy.[83]

Frequency calculations were performed only for the absorbates (in gas phase and adsorbed) at the same level of theory except that a Fermi smearing of 0.1 eV was used. Using these frequencies, the zero-point corrected enthalpy (H) and free energy (G) were calculated using the usual thermochemistry and statistical mechanics approximation.

Nanoparticles Optimization and Reactivity

While there are several reports regarding the interaction of clusters with surface,[84–92] modeling the interaction between nanoparticles (at least one nanometer large) and a surface, especially if the latter is an amorphous surface such as silica is a real modeling challenge. Born−Oppenheimer (BO) *Ab Initio* Molecular Dynamic (AIMD) with annealing at high temperatures (*vide infra*) was used to explore the conformational space of Pt and PtGa nanoparticles (37 atoms, 1 nm diameter) on silica surfaces, starting from the vacuum optimized nanoparticles deposited on silica or Ga-doped silica surface. To do the AIMD simulations we used CP2K[93,94] with the rev-PBE functional[75–78] completed with additional D3-BJ dispersion corrections,[23] the single-ζ GPW basis set for the support (SiO_2 and D of the support), and the double-ζ GPW basis set on Pt, Ga, and the C and D atoms of propane together with their respective associated GTH pseudopotentials.[95–98] The system was first equilibrated using the NVT ensemble for 3 ps with a 1.0 fs step, using a 875 K velocity-scaling thermostat which corresponds to the working temperature to synthesize these catalysts. To access larger time steps, all H atoms were replace by D atoms. Then the most stable structures generated during annealing were slowly cooled over 2 ps using a velocity rescaling factor of 0.999 (see the [SI] for temperature and energy evaluation with time).

The following energy-based indicators were used to described the interaction of the nanoparticle with the surface (i) interaction energy of the nanoparticle with the surface

$$E_{tot} = E_{NP\text{-}on\text{-}surface} - (E_{NP\text{-}in\text{-}vacuum} + E_{surface})$$

(ii) deformation energy between nanoparticle in vacuum and nanoparticle on surface;

$$E_{def} = E_{distorted\text{-}NP} - E_{NP\text{-}in\text{-}vacuum}$$

(iii) interaction energy between the distorted nanoparticle and surface:

$$E_{int} = E_{tot} - E_{def}$$

Number of closest neighbors or number of bonds used in this study are defined assuming that there is a bond if and only if is the distance between the two atoms is less or equal to the half sum of the atomic distances of the two atoms.

Metadynamics (MTD)

The AIMD parameters were similar to the ones used in the previous part (see above). The free energy surface (FES) was explored by means of metadynamics,[67−70] using a history dependent potential applied along selected collective variables (CVs) to describe the dehydrogenation mechanism. This potential takes the following form:

$$V(t, s(t)) = w \sum_n e^{-(1/2)(s(t)-s(n \cdot t_G)/\delta_G)^2}$$

with w = 0.001 a.u. and δ_G = 0.2, respectively, being the height and width of the Gaussian and t_G = 10 fs being the time interval between two consecutive Gaussian hills.

CVs must be selected in order to distinguish between reactant and product state while including slow relaxation modes. For PDH C to D and C to Pt coordination numbers (CN) were considered, and C−C distance was included in the case of coking. CNs are defined as follows:

$$CN_{AB} = \sum_{i_B} \frac{1 - \left(\frac{r_{i_A}}{R_0}\right)^{nn}}{1 - \left(\frac{r_{i_A}}{R_0}\right)^{nd}}$$

where nn = 6, nd = 12, and R_0 corresponds to the AB bond distance, and takes 1.6 Å for the C−D bonds and 2.3 Å for the C−Pt ones. These R_0 values are based on the respective optimized bond lengths in the related transition state structures obtained from static DFT.

3. EXPERIMENTAL SECTION

The molecular complexes $[Ga(OSi(OtBu)_3)_3(THF)]$[51] and $[Pt(OSi-(OtBu)_3)_2(COD)]$[99] were prepared according to a literature procedure. The material $Pt(OSi(OtBu)_3)(COD)\_Ga/SiO_2$ and $PtGa/SiO_2$ were likewise prepared according to a reported procedure.[18]

Synthesis of PtGa/SiO₂_100

$Pt(OSi(OtBu)_3)(COD)\_Ga/SiO_2$ was added to a tubular quartz flow-reactor supported with a porous quartz frit. The reactor was heated to 100 °C (ramp of 5 °C/min) and kept at that temperature for 1 h under a steady flow of H_2. The reactor was subsequently evacuated under high vacuum (10^{-5} mbar) while cooling to room temperature (rt). A dark material was obtained which was transferred to an argon filled glovebox. Half of the material was reheated to 100 °C (ramp of 5 °C/min) and kept at that temperature for 10 h. Evacuation was done under the same conditions as mentioned before to obtain $PtGa/SiO_2\_100$ as a black material.

X-ray Absorption Spectroscopy (XAS)

XAS measurements were carried out at the Ga K-edge and Pt L_3-edge at the SuperXAS beamline at SLS (PSI, Villigen, Switzerland). The storage ring was operated at 2.4 GeV in top-up mode with a ring current of around 400 mA. The incident photon beam provided by a 2.9 T superbend magnet was selected by a water-cooled Si(111) quick-EXAFS monochromator, and the rejection of higher harmonics and focusing were achieved by a rhodium-coated collimating mirror at 2.5 mrad and a rhodium-coated toroidal mirror at 2.5 mrad. The beamsize on the sample was 1200 μm × 200 μm. During measurements, the

monochromator was rotating with 1 Hz frequency in 2 deg angular range, and X-ray absorption spectra were collected in transmission mode using ionization chambers specially developed for quick data collection with 1 MHz frequency.[100] The spectra were collected for 5 min and averaged. The beamline energy was calibrated with a Pt reference foil to the Pt L_3-edge position at 11564 eV. To avoid contact with air, all samples were sealed in a glovebox. For ex situ samples, pressed pellets (with optimized thickness for transmission detection) were placed in two aluminized plastic bags (Polyaniline (15 μm), polyethylene (15 μm), Al (12 μm), polyethylene (75 μm) from Gruber-Folien GmbH & Co. KG, Straubing, Germany) using an impulse sealer inside a glovebox; one sealing layer was removed immediately before the measurements. Data processing was done by standard procedures using the ProXASGui software package developed at the SuperXAS beamline, PSI, Villigen. The program package Demeter was used for data analysis.[101] S0^2 values for the Ga K edge were obtained by fitting $Ga(acac)_3$ with fixed coordination numbers according to crystal structure data.

4. RESULTS AND DISCUSSION

4.1. Structure of PtGa Supported Nanoparticles

4.1.1. Interaction of Pt Nanoparticle with SiO_2 and Ga-Doped SiO_2 Surfaces. The AIMD annealing sequence and the subsequent gradient optimization (see the Computational Section) were used to optimize a set of realistic-size[18] Pt-based nanoparticles to probe the effect and the role of the oxide support on the structure and the shape of Pt-based nanoparticles (Figure 1). We considered nanoparticles (1 nm, 38 atoms) interacting with three model amorphous surfaces (Figure 2 and Figure S3): two amorphous silica models[102] developed earlier to mimic dehydroxylated silica ("$SiO_{2\text{-}700}$", 1.1 OH nm^{-2}) and hydroxylated silica ("SiO_2", 7.2 OH nm^{-2}) and a model of Ga^{III}-doped dehydroxylated silica ("Ga/$SiO_{2\text{-}700}$", 1 Ga nm^{-2}; 1 OH nm^{-2}).[103] To evaluate the impact of the initial configuration on the optimized structure and associated energy, two different starting points were optimized in the case of $SiO_{2\text{-}700}$ (Figure S4). Both the initial structures and the chosen oxide surfaces have an impact on the obtained global energy. Thus, only trends between different surfaces are considered while absolute interaction energies between the nanoparticle and the oxide support are not discussed. A summary of these results is depicted in Figure 2 (see Figures S4−S6 for the complete set of optimized structures); in each case, the average deformation energy (E_{def}) of the nanoparticle, the interaction energy (E_{int}), and total stabilization energy (E_{tot}) are reported based on six structures (see the Computational Section for a definition of these indicators).

Starting from a vacuum optimized Pt nanoparticle deposited on silica, the average number of Pt−O bonds increased to an average value of 9.0 for a highly dehydroxylated silica $SiO_{2\text{-}700}$ and of 2.5 for hydroxylated SiO_2 (see Figure S7), due to the insertion of Pt atoms into elongated Si−O bonds. The contrast between Pt supported on SiO_2 and $SiO_{2\text{-}700}$ is striking: the low affinity of Pt for SiO_2 (E_{int} = −122 kcal mol^{-1}) leads to a quasi-spherical nanoparticle structure (Figure 2, E_{def} = +40 kcal mol^{-1}) while on $SiO_{2\text{-}700}$ the flattening is significant (Figure 2, E_{def} = +147 kcal mol^{-1}) due to the strong interaction with the dehydroxylated support (E_{int} = −156 kcal mol^{-1}). The interaction of a Pt nanoparticle with a Ga-doped silica surface was also investigated. Similar to $SiO_{2\text{-}700}$, the Pt nanoparticle is significantly flattened compared to gas phase optimization (Figure 2, E_{def} = +107 kcal mol^{-1}), but having a much more favored interaction with the surface and nearly doubled E_{tot} (E_{int} = −265 kcal mol^{-1}).
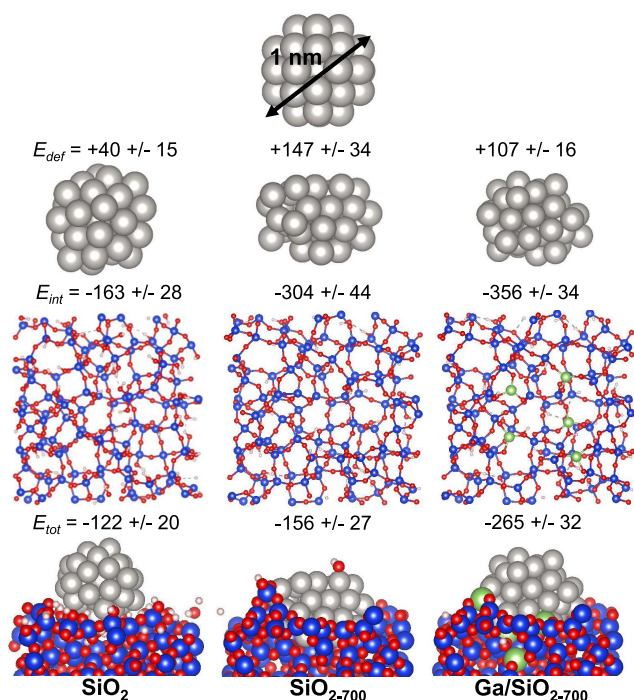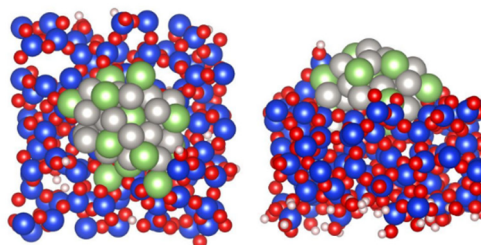
Figure 2. Interaction of SiO$_2$, SiO$_{2\text{-}700}$, and Ga-doped SiO$_{2\text{-}700}$ surfaces with Pt 38-atoms (1 nm) nanoparticles. The most stable structure obtained for each case is depicted (see the SI for the complete set of structures, Figures S4−S6). Average values on all optimized structures of interaction energy of the nanoparticle with the surface (E_{tot}); deformation energy between nanoparticle in vacuum and nanoparticle on surface (E_{def}); interaction energy between the distorted nanoparticle and surface (E_{int}), the variability (indicated by ±, see the Computational Section for a complete definition of these values) was estimated by reporting the standard deviation, all values are in kcal mol^{-1}. Conventions: Si (blue), O (red), H (white), Pt (gray), Ga (green).

To facilitate the molecular understanding on the interaction between Pt and the support, the interaction of a single Pt atom with SiO$_{2\text{-}700}$ and Ga/SiO$_{2\text{-}700}$ surface sites was also considered (see the Supporting Information for details, section 3). Pt^0 atoms can insert into distorted Si−O bonds and the interaction energy follows the bond elongation (−19.9 kcal mol^{-1} for a nondistorted bond up to −93.4 kcal^{-1} for the most elongated one, averaged energy −20.7 kcal mol^{-1}; Figures S8−S9). This trend allows an explanation of the difference of behavior modeled between a hydroxylated and a dehydroxylated silica surface: SiO$_{2\text{-}700}$ is distorted and displays a high number of reactive elongated Si−O bonds compared to SiO$_2$.[102]

Pt^0 atoms interact strongly with Ga^{III} sites with an average interaction energy (−60.6 kcal mol^{-1}, Figure S11) that is much higher than in the case of pure silica. This interaction leading to the partial breaking of the Ga−O bond is due to the donation of the Pt^0 to the vacant p orbital of Ga^{III} and back-donation of the O lone pair (Figure S8). Evidence for the interaction between Pt^0 and Ga^{III} centers is in fact experimentally evidenced (vide infra). As expected, the trend obtained on single atoms interaction with model sites mimics the one obtained with real size nanoparticles interacting with surfaces. These results are also in agreement with the experimental finding that the average size of SOMC-generated Pt-nanoparticles is lower on highly dehydroxylated silica (SiO$_{2\text{-}700C°}$)[104] than on partially dehydroxylated one (SiO$_{2\text{-}200C°}$) and even more in the presence of Ga^{III} sites,[18] and explain the high stability of this system toward sintering.

4.1.2. Structure Refinement and Formation Mechanism of PtGa Nanoparticles Supported on Ga-Ddoped SiO$_{2\text{-}700}$.

As already alluded to in the Introduction, it has so far been difficult to obtain a molecular-level understanding of the structure of the PtGa nanoparticles. Another unsolved issue is the mechanism of formation of such alloyed nanoparticles. Previously obtained XPS and EXAFS data for these supported PtGa nanoparticles seem to contradict each other: while XPS indicates that a large proportion (up to 90%) of Ga behaves as Ga^0, EXAFS data suggest a Ga−O coordination number of 1.4, which would correspond to 50% of Ga^{III} remaining at the support surface, assuming three Ga−O bonds *per* Ga^{III}.[18] This surprising result prompted us to study the structure of Pt$_2$Ga nanoparticles in more detail using AIMD. Before optimization, the initially guessed geometry, spherical 1 nm Pt$_2$Ga nanoparticles (1 nm, 12 Ga, and 26 Pt) deposited on a Ga-doped SiO$_2$ surface (1 Ga *per* nm^2), agreed with XPS data (roughly 10% of Ga^{III} acid sites and 90% of Ga^0 incorporated in the nanoparticle), but lay far from the EXAFS analysis (0.2 Ga−O bonds *per* Ga). The optimized structure reveals the movement of Ga^0 toward the surface of the nanoparticle and the corresponding interaction of the surface Ga^0 with the silica support, strongly interacting with the Si−O bonds, similarly to what we described earlier for the case of Pt atoms (Figure 3 and

**Figure 3.** Interaction of Ga-doped SiO$_{2\text{-}700}$ surfaces with Pt$_2$Ga 38-atoms (1 nm) nanoparticles. The most stable structure obtained for each case is depicted (see the SI for the complete set of structures, Figure S12). Conventions: Si (blue), O (red), H (white), Pt (gray), Ga (green).

Figure S12). Thus, as a result, Ga atoms strongly interact with the oxide surface leading to an average number of Ga−O bonds increased by a factor of 10 to an average value of 2.1 Ga−O *per* Ga atom (Figure S13). As such, the obtained optimized structure is consistent with both EXAFS (high number of Ga−O bonds) and XPS data (oxidation state of Ga).

We then further explored the formation process of the PtGa alloy using *ex situ* and *in situ* XAS spectroscopy by monitoring the reaction of Pt(OSi(OtBu)$_3$)(COD)_Ga/SiO$_2$ under a flow (1 bar) of H$_2$ (from ambient temperature to 550 °C, Figures S14−S15).

The *in situ* data support the sequential reduction of Pt and Ga according to at the Pt L3-edge and Ga K-edge, respectively. Linear combination fitting (LCF) analysis was used to evaluate the proportion of remaining Pt^{II} and Ga^{III}: while Pt^{II} is reduced very quickly and almost fully, even at room temperature, the reduction of Ga^{III} only takes place at ca. 200 °C (Figure S15). This sequential reduction should allow for the isolation and characterization of intermediate states of the system. As a transient state, almost all Pt is reduced while the large majority of Ga remains as isolated Ga^{III} sites, paralleling what has been reported for similar materials, for example, Pt/Ga modified zeolites.[105,106] We concluded that a more detailed character-

ization of such intermediate states *via ex situ* XANES and EXAFS would provide complementary information and a more detailed understanding of the formation mechanism. Thus, a sample was prepared by H_2 treatment of $Pt(OSi(OtBu)_3)(COD)\_Ga/SiO_2$ at low temperature (PtGa/SiO$_2$_100, 100 °C, 10 h, see the Experimental Section) and evaluated *ex situ* in order to obtain higher quality EXAFS data for a detailed analysis. Under these conditions, EXAFS analysis at the Ga K edge shows that the number of Ga–O nearest neighbors is comparable to the one in the initial state of the material $Pt(OSi(OtBu)_3)(COD)\_Ga/SiO_2$ (Figure 4, Tables S6–S8), while the LCF of the Ga K-edge
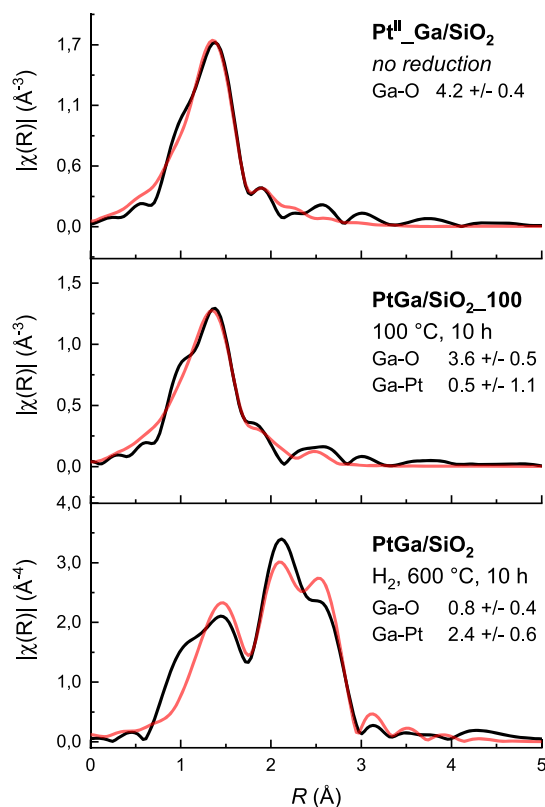

Figure 4. EXAFS data (black) and fits (red) in R-space in Ga K-edge of (top) $Pt(OSi(OtBu)_3)(COD)\_Ga/SiO_2$ (=Pt^{II}–Ga/SiO$_2$) (middle) PtGa/SiO$_2$_100 and (bottom) PtGa/SiO$_2$ (see Tables S6–S8 for optimized parameters).

XANES spectrum of this material indicates that around 10% of Ga^{III} was reduced at this stage (Figure S16). Attempts to fit a Ga–Pt pathway leads to small coordination numbers with large error (Ga–Pt CN = 0.5 ± 1.1), which might suggest a low amount of Ga–Pt interaction with either alloyed Ga^0 or Ga^{III} surface sites. (see SI for more detail).

We then investigated the material at the Pt L$_3$ edge. Both LCF of the XANES spectrum and fitting of the EXAFS region confirmed the almost complete reduction of Pt at 100 °C (Figure S17 and Table S3). Fitting of the Pt–Pt path indicates an average low-number of neighbors (5.5 ± 0.7) that is consistent with the formation of Pt clusters or very small Pt nanoparticles. This observation agrees with the transmission electron microscopy (TEM) images of the sample indicating clusters or particles below 1 nm (Figure S18). Inclusion of other pathways such as Pt–O or Pt–Ga did not improve the fit. Considering the above data for PtGa/SiO$_2$_100, the intermediate state in the formation of the final material likely

corresponds to small Pt nanoparticles/clusters, interacting with a small amount of incorporated Ga^0 and surface Ga^{III}-sites. Further increasing the temperature during thermal treatment led to the reduction and increased incorporation of Ga^{III} from the interface into the Pt nanoparticle, leading to a more Ga enriched PtGa nanoparticle as described before.[18]

4.1.3. Dynamic Structure and Property of the Supported Nanoparticles of Pt vs Pt$_2$Ga.

The previously optimized Pt and Pt$_2$Ga nanoparticles were equilibrated for 1 ps at 875 K. Pt and Pt$_2$Ga nanoparticles behave very differently: while the pure Pt particle displays low atomic motion, the Pt$_2$Ga nanoparticle displays high mobility and disorder, behaving like a melted droplet. This can be easily pictured by looking at the overlapped positions of the atoms along the simulation time (Figure 5) or alternatively by looking at the histogram of Pt–Pt
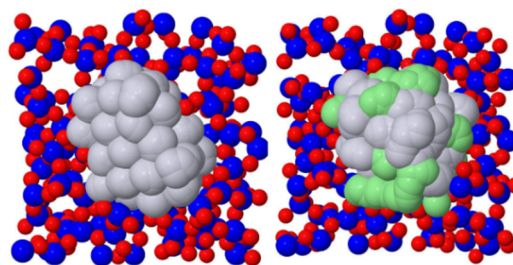

Figure 5. Time evolution (1 ps, superimposed pictures) of the structure of Pt (left) and Pt$_2$Ga (right) silica supported nanoparticles obtained by AIMD. Conventions: Si (blue), O (red), H (white), Pt (gray), Ga (green).

distances in both cases (Figure S19). In the case of pure Pt nanoparticle (Figure 5, left), one can still see the characteristic hexagonal pattern associated with the (111) facet while a less clear pattern is visible in the case of Pt$_2$Ga (Figure 5, right). Looking at the bond histogram (Figure S19), the shortest Pt–Pt distance is elongated in Pt$_2$Ga compared to the case of pure Pt (2.71 vs 2.66 Å, respectively) and the long-range organization (corresponding to the second coordination sphere) is very broad in Pt$_2$Ga compared to Pt.

4.2. Activity of Pt$_2$Ga Supported Nanoparticles

We were curious to understand how such subtle changes in the nanoscale structure of the catalyst could influence the activity and to decipher the effect of the NP/surface interface on activity. Efficient exploration of the free energy surface (FES) for such large systems can be performed using metadynamics to accelerate the sampling process (see computational details). The results obtained from MTD (section 2.1) are then compared in a subsequent section (section 2.2) with static calculations of periodic surfaces to obtain more insights into the various effects influencing the activity.

4.2.1. Metadynamics Simulations of PDH on SiO$_2$-Supported Pt and Pt$_2$Ga Nanoparticles.

The reactivity of PtGa$_2$ and Pt nanoparticles supported on SiO$_2$ and Ga-doped SiO$_2$-700$ was studied by metadynamics simulations. Here follows the list of collective variables (CVs) that were used to study PDH (Figure 6A,D): C1 (terminal carbon) to H coordination numbers (CV1), C2 (central carbon) to H coordination number (CV2), C1 to all Pt coordination number (CV3), and C2 to all Pt coordination number (CV4). Evolution of the CVs in the case of PDH on a SiO$_2$-700$ supported Pt nanoparticle is displayed in Figure 6A. C–H activation of the terminal C–H bond is taking place at ca. 1100 fs (Figure 6A) as indicated by the sharp
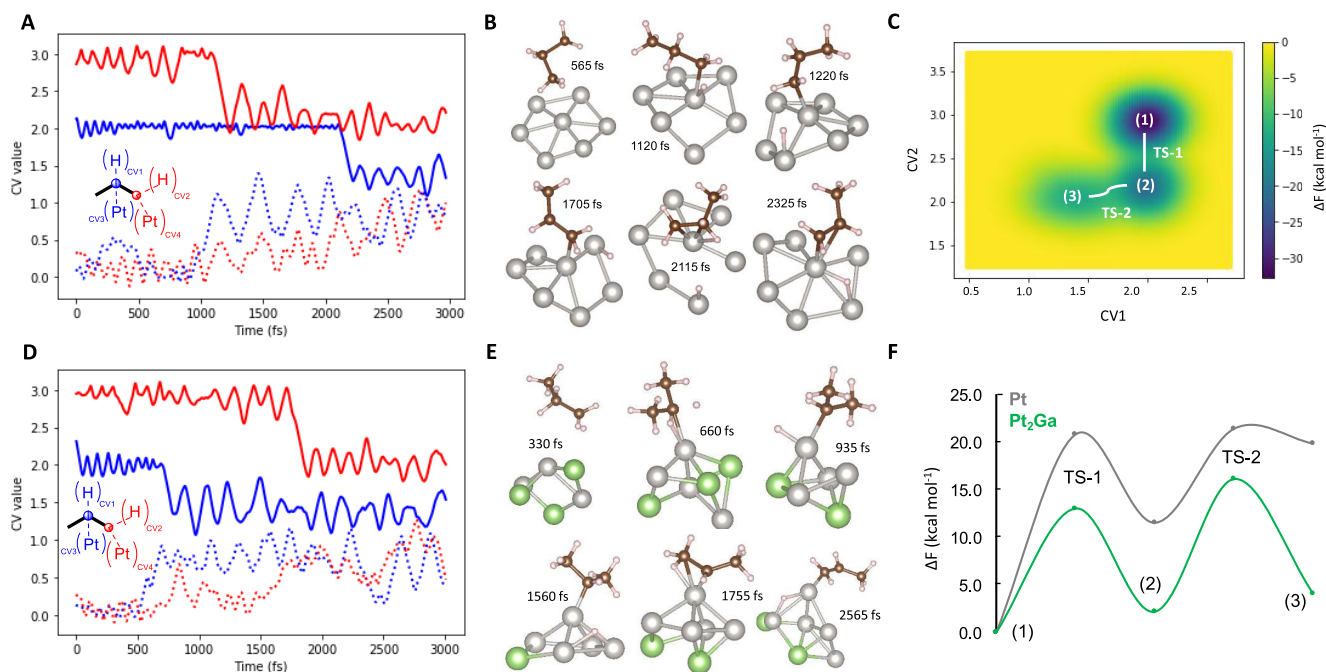
Figure 6. (A) Evolution of CVs as a function of time (CV1 blue line, CV2 red line, CV3 blue dots, CV4 red dots) during PDH metadynamics simulation on SiO_{2-700} supported Pt nanoparticle. (B) Snapshot of the movie of PDH metadynamics simulation on SiO_{2-700} supported Pt nanoparticle (see Figure S25 for snapshot of the complete system). (C) FES of PDH on SiO_{2-700} supported Pt nanoparticles as a function of CV1 and CV2 as reconstructed from the metadynamics run (see Figures S27 for FES as a function of CV1−CV3 and CV2−CV4). (D) Evolution of CVs as a function of time (CV1 blue line, CV2 red line, CV3 blue dots, CV4 red dots) during PDH metadynamics simulation on Ga-doped SiO_{2-700} supported Pt_2Ga nanoparticle. (E) Snapshot of the metadynamics movie (see Figure S29 for snapshot of the complete system). (F) Helmholtz free energy (ΔF, kcal mol^{-1}) at 875 K pathways for PDH on SiO_{2-700} supported Pt and Pt_2Ga and Pt nanoparticles obtained from metadynamics run (see Figure S28 for FES for the PdGa system as a function of CV1 and CV2). (1) adsorbed propane; TS-1 first C−H activation; (2) Pt-alkyl intermediate TS-2 s C−H activation; (3) adsorbed propene. Movies of the simulations are available in the SI.

decrease of H coordination number on C2 (CV2) from 3.0 to 2.0. This step occurs in a concerted way, as evidenced by the concerted increase of CV4 (Pt coordination number to C2) from 0.0 to 1.0. Thus, overall, this is consistent with the concerted breaking of one C−H bond and formation of a new C−Pt bond (Figure 6B). This step is taking place on an heptacoordinated Pt atom located in the center of a distorted Pt hexagon similar to the one observed on Pt the (111) facet (Figure 6B, 1120 fs). The formed Pt-hydride is quickly migrating away from the Pt-alkyl moiety (Figure 6B, 1220 fs). The formation of Pt-alkyl induces a distortion of the Pt surface (Figure 6B, 1705 fs), with the Pt bonded to C located significantly out of the plane of the surface. The second C−H activation is taking place on the same Pt atom around 2100 fs as indicated by the variation of CV1 from 2 to 1 and yields a π-coordinated propene (as indicated by CV3 and CV4 converging to an average value of 0.5) while the second hydride quickly diffuses away (Figure 6B 2115 and 2325 fs).

The complete FES parametrized by the chosen CVs can be reconstructed from the sum of the Gaussian potentials (Figure 6C).[67−70] The position of intermediates and TSs are indicated on Figure 6C, featuring the FES as a function of (CV1,CV2): propane corresponds to the position (2,3), the Pt-alkyl intermediate corresponds to (2,2), and propene to (1,2); transition states are located around (2,2.5) and (1.5,2) respectively. Minimum energy pathways (MEPs) connecting to minima can be obtained from the FES (Figure 6F, see Figure S26 for comparison with results obtained from static calculations on periodic surfaces).

Evolution of the CVs in the case of PDH on a Ga-doped SiO_{2-700} supported Pt_2Ga nanoparticle is displayed in Figure 6D. C−H activation of the central C−H bond takes place around 600 fs (Figure 6E) with the simultaneous formation of one C−Pt and one H−Pt bond on the same unsaturated Pt atom (with four Pt neighbors vs seven for the active site of supported Pt nanoparticle) located on top of a distorted Pt square pyramid (Figure 6E). Migration of the formed Pt-hydride is blocked by the distortion of the surface and the presence of Ga atoms (as formation of Ga hydride is highly disfavored). The second C−H activation occurs around 1750 fs, on the same pseudoisolated Pt-center, and yields π-coordinated propene (Figure 6E). Both C−H activation steps take place on a highly unsaturated Pt.

As already mentioned, the Pt_2Ga nanoparticle features high mobility and is thus strongly distorted. The average coordination number at 875 K is around 9, while it is around 10 for supported Pt nanoparticles. This is in agreement with the static calculation results, indicating that the adjunction of Ga favors the formation of the corrugated (111) facet featuring unsaturated Pt centers (see section 2.2).

In general, this combination of high mobility−allowing for the stabilization of intermediates−and distortion−favoring the existence of unsaturated active sites is expected to favor higher activity. Indeed, comparison of the MEPs obtained by MTD for Pt and Pt_2Ga nanoparticles (Figure 6F) revealed that PDH is predicted to have a lower free energy (Helmholtz energy) barrier of activation on Pt_2Ga than on Pt (Figure 6 and Figure S26, energy span of 25.9 vs 29.6 kcal mol^{-1}), suggesting higher activity of PtGa based catalysts.[107,108]
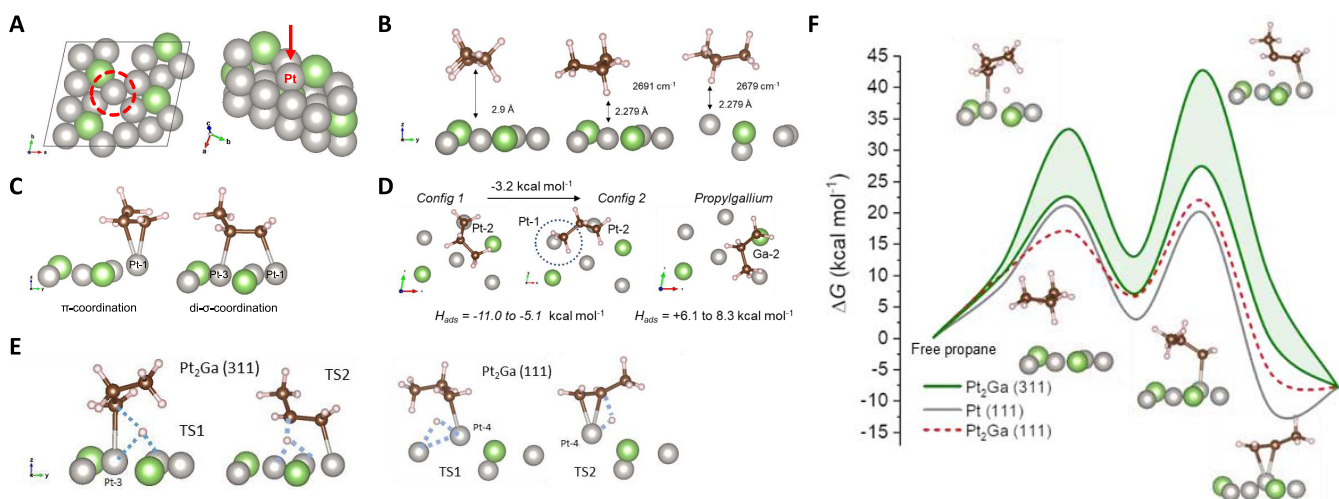
Figure 7. (A) Pt_2Ga (111) surface; adsorption mode of propane (B), propene (C), and propyl (D); most stable transition state corresponding to the first C H activation step (E) on PDH on the Pt_2Ga surface; (F) lowest and highest optimized free energy at 875 K (kcal mol^{-1}) pathways for PDH on Pt_2Ga (311) (both in green) and lowest energy pathway for PDH on Pt_2Ga (111) (dashed red) and on Pt (111) surface (gray) (see Figures S23 for enthalpy pathways).

4.2.2. Static Simulations of PDH on Model Surfaces.

We were curious to contrast these results from MTD with modeling based on static calculation on periodic surfaces. The comparison would allow us to discriminate between electronic and surface effects and the ones related to nanoparticle disorder and mobility. The surface energies corresponding to the most stable bulk structure of the Pt_2Ga alloy were calculated (Table S2, Figure S2). The two most stable surfaces are the (111) and the (311) facets (Figures 1 and 7A) with surface energies of 0.93 J m^{-2} and 0.99 J m^{-2}, respectively. Similar to what is observed in the bulk, Ga^0 is also very dispersed on these surfaces, and no Ga^0 atoms are close to each other. While the (311) facet is a flat surface that displays the stoichiometry of the alloy (Pt/Ga, 2:1), the (111) facet is Pt enriched (3:1) and corrugated, featuring out-of-plane unsaturated Pt atoms (Figure 7A). The activity of the Pt_2Ga (311) and (111) facets was first studied in detail and the Pt (111) surface was also evaluated for comparison purpose using static calculations (see computational details). The Pt_2Ga (311) facet was used as a reference surface where all possible pathways were calculated, while only the more active out-plan Pt-4 was considered on the Pt_2Ga (111) facet (Figure 7A). For comparison, the activity of the (012) Pt_2Ga surface, the most stable surface obtained from the experimentally reported Pt_2Ga XRD-structure,[34] was also estimated and proven similar to the one of the *ab initio* optimized (311) surface (see Table S21).

The calculated adsorption enthalpy of propane on the Pt_2Ga (311) surface comprises between −9.4 and −11.1 kcal mol^{-1} (Table S9), close to the adsorption energies on the Pt (111) facet (−11.7 kcal mol^{-1}; experimentally, −10.2 kcal mol^{-1}).[109] Two configurations are found for adsorbed propane (Figure 7B): (i) propane interacting with the surface only through dispersion forces and (ii) a propane σ-complex on a surface Pt-atom; the latter being slightly more favored than the former (−9.4 kcal mol^{-1} vs −11.1 kcal mol^{-1}). Adsorption on the Pt_2Ga (111) facet is significantly more favored (−15.4 kcal mol^{-1}) due to the bonding with the unsaturated Pt-4 (Figure 7B).

For propene adsorption on the (311) Pt_2Ga facet, several conformations (Figure 7C, see Table S10−S11 for the complete set of optimized structures) are possible and were optimized, involving single (π-coordination, Pt-x with $x = 1−4$, $\Delta H_{ads} =$

−13.7 to −22.6 kcal mol^{-1}, see Figure 7A for numbering of Pt atoms) as well as di-σ-coordination (Pt-x−Pt-y $x = 1−4$, $y = 1−4$, $\Delta H_{ads} = −14.9$ to $−24.6$ kcal mol^{-1}). While σ-coordination is preferred at low temperature, it is entropically less favorable than the π-coordination. Thus, the free energy difference between both coordination modes decreases with temperature (Tables S8−S9) and becomes negligible at 875 K. Coordination to the Ga surface sites is never favorable; in fact, any attempt to optimize adsorbed propane on Ga sites always leads to coordination to Pt sites.

These energies have to be compared to what is obtained on the pure Pt (111) surface. On this latter surface, propene adsorption energy is significantly higher than on the Pt_2Ga system and dicoordination of propene is favored compared to the monocoordination mode, $\Delta H_{ads} = −24.5$ kcal mol^{-1}, vs π-coordination, $\Delta H_{ads} = −32.7$ kcal mol^{-1}, but this trend is reversed at 875 K ($\Delta G_{ads} = −11.5$ vs $−6.7$ kcal mol^{-1}) due to the entropic contribution. Overall, the introduction of Ga decreases the affinity of alkenes for Pt and as found in the case of Sn in PtSn catalyst.[34−40] Part of the lower affinity of propene for Pt_2Ga is due to geometric effects coming to the adjunction of Ga atoms to the Pt, which increases the distance between Pt atoms thus disfavoring the di-σ adsorption mode on Pt and partially to electronic effects (see the SI comments associated with Figures S20−S22).

This model holds true for flat surfaces; however, the distorted and unsaturated Pt_2Ga (111) surface—lower in energy than the (311)—is likely to have a different behavior. The particular activity of step sites was underlined for Pt.[39] Structures and energies of propene adsorbed on Pt_2Ga (111) are provided in Tables S8 and S9. Both σ (−23.9 to −26.8 kcal mol^{-1}) and π-coordination of propene (−20.4 to −31.4 kcal mol^{-1}) are significantly more favored compared to adsorption of the flat (311) surface and close to the one on Pt (111) (Tables S8 and S9). At 875 K the entropic contribution dominates and the π-coordination is favored, as found for pure Pt. This agrees with the results from AIMD showing a preferred π-coordination at 875 K (Figure 6D,E).

The mechanism of PDH on Pt (111) and Pt_2Ga (311) was subsequently investigated (Figure 7). Starting from propane,
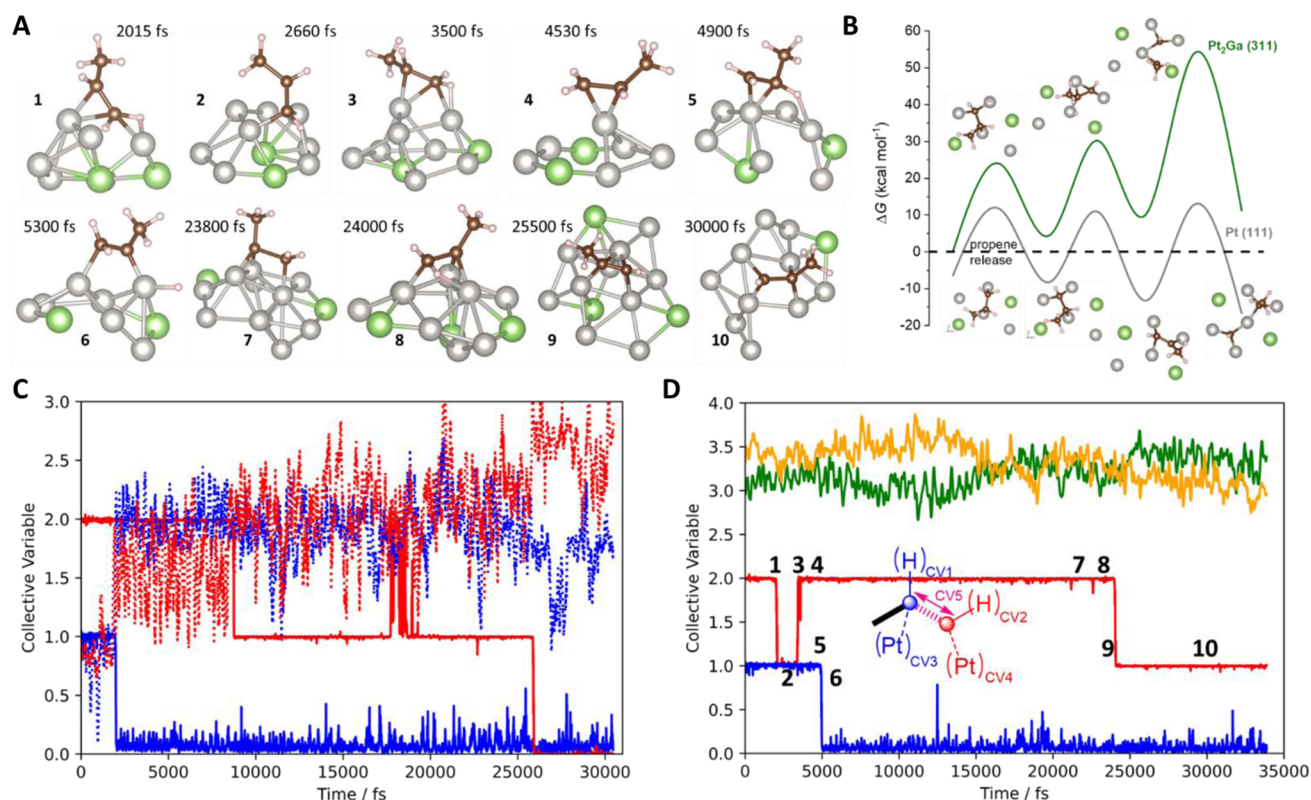
Figure 8. (A) Snapshots of the movie of the coking metadynamics simulation on Ga-doped SiO_{2-700} supported Pt_2Ga nanoparticle (see Figure S31 for snapshot of the complete system). (B) Gibbs Free energy (kcal mol^{-1}) pathway for propene deep dehydrogenation and coking on (311) Pt_2Ga surface (red) and on pure (111) Pt (blue) (see Figure S24 for enthalpy pathways, only the lowest energy path is represented, see Tables S16−S20 for other paths). (C) Evolution of CVs as a function of time (CV1 blue line, CV2 red line, CV3 blue dots, CV4 red dots) during PDH metadynamics simulation on SiO_{2-700} supported Pt nanoparticle. (D) Evolution of CVs as a function of time (CV1, blue line; CV2, red line; Pt−Ga coordination number, orange line; Pt−Pt coordination number, green) during PDH metadynamics simulation Ga-doped SiO_{2-700} supported Pt_2Ga nanoparticle. Collective variables were reconstructed after simulation using different parametrization (see SI) using plumed software[111,112] for the sake of visualization.

C−H bond activation on surface Pt atoms yields the propyl intermediate (Figure 7D). As for propene coordination, all possible propyl intermediates on the Pt_2Ga surfaces were computed (Figure 7D, Table S12 for alternative structures and energies). While the surface propyl-gallium intermediate could be optimized, all structures lie relatively high in energy (Figure 7D, +6.1 to +8.3 kcal mol^{-1} vs −11.0 to −5.1 kcal mol^{-1} for propyl-platinum intermediates), excluding the direct participation of Ga in the C−H activation step. Propyl-platinum intermediates can adopt two different conformations, with or without supplementary Pt−H−C interaction (Figure 7D), the second one being slightly favored (−3.2 kcal mol^{-1}). As expected, unsaturated Pt-4 on distorted Pt_2Ga (111) allows stabilizing (−10.9 kcal mol^{-1}) the propyl intermediate. Compared to the same species adsorbed on the Pt (111) surface all optimized intermediates are higher in energy on Pt_2Ga (−11.0 vs −15.3 kcal mol^{-1} on Pt). This is in contrast with what is obtained from AIMD, for which the reorganization of the NP leads to a very stable propyl intermediate (Figure 6F).

The two C−H activation steps take place via the concerted insertion of a Pt atom into the C−H bond and migration of a H atom on another Pt site (Figure 7E); thus at least two adjacent Pt sites would be required. Once again Ga sites cannot play an active role in this process since the formation of Ga hydride is not favored (see Table S13 for all possible hydride optimized structures, any attempt to optimize Ga-hydride leads to the migration of the hydride on one adjacent Pt). All possible transition states for this insertion on the (311) surface were

optimized (Figure 7E and Table S14). With stability ranging between (+4.0 and +9.6 kcal mol^{-1}), the activation energy for this step is always higher on Pt_2Ga than on Pt (+3 kcal·mol^{-1}). Remarkably, C−H activation taking place on the unsaturated Pt-4 atom of the Pt_2Ga (111) facet is highly favored (−1.7 kcal mol^{-1}, Figure 7E) with an activation enthalpy lower than the one obtained on Pt (111) (+3.0 kcal mol^{-1}).

Similarly, several transition states were optimized for the second C−H activation, yielding adsorbed propene (Figure 7E, Table S15). The same trend was obtained for this step, the transition state being always significantly higher in the case of Pt_2Ga (311) compared to Pt (111) (+4.8 vs −1.8 kcal mol^{-1}, respectively, see Table S15). However, the Pt_2Ga (111) surface shows PDH activity comparable to the one of Pt (111) (−1.7 kcal mol^{-1}, Figure 7). The dispersion of Pt and the low coordination of the Pt-4 site favor the β-H transfer step to form directly π-coordinated propene.

The various free energy pathways for PDH on Pt (111) and Pt_2Ga (311) and (111) are displayed in Figure 7F. The general trend is that all adsorption energies are weaker on Pt_2Ga compared to Pt, resulting in both lower activation energies for C−H activation and a higher propene desorption energy for Pt compared to Pt_2Ga. However, this is true only for flat surfaces (311) where electronic effects predominate. On a distorted (111) surface the presence of Ga favors the formation of unsaturated highly active Pt single sites (Pt-4) featuring higher or similar activity compared to Pt (111).

Finally, AIMD simulations predict higher PDH activity for Pt$_2$Ga compared with Pt, while the trend is rather reversed compared to static calculations with Pt$_2$Ga showing similar or lower activity compared to pure Pt (Figure 7F). However, due to these two above-described opposite effects (electronic vs geometric) it is hazardous to conclude on the activity trend between Pt and Pt$_2$Ga based only on static periodic DFT calculations. Comparisons between free energy pathways obtained from metadynamics and static DFT are display in Figure S26. Compared to the static free energy pathway the general profile does not change but free energies of activation obtained by metadynamics are higher, likely due to under-estimation of entropy effects in static calculations.

4.2.3. Coke Formation on SiO$_2$-Supported Pt and Pt$_2$Ga Nanoparticles.
The main pathway leading to the deactivation of Pt based catalysts under PDH conditions is the formation of coke.[38−40] This reaction requires the cleavage of C−C bonds, which is facilitated by deeper dehydrogenation of the substrate, that is, formation of alkynes, which are in turn more easily activated than a single C−C bond, as previously demonstrated on related systems.[38−40] We thus also explored the formation of propyne and its subsequent cracking as a simple model for coke formation pathways (Figure 8).

To model the coking pathway, the following CVs were considered starting from adsorbed propene: hydrogen and platinum coordination to central and middle carbons (CVs 1−4 as defined above) as well as the distance between central and middle carbon (CV5, Figure 8D). This set of CVs is expected to limit the bias added to the system, that is, no specific order between possible C−H and C−C activation is imposed and metadynamics should allow to localize the most favorable pathway. Evolution of the CVs in the case of the SiO$_{2-700}$ supported Pt nanoparticle is displayed in Figure 8C (see SI Figures S30 and S31, for snapshots). Starting from propene (CV1 = 1 and CV2 = 2), activation of the middle C−H group takes place after 2000 fs (decrease of CV1 from 1.0 to 0.5), simultaneously CV3 and CV4 increase revealing the formation of a Pt tricoordinated intermediate, in agreement with the structures optimized using static DFT (Figure 8C). Sequentially, activation of the terminal C−H group occurred around 8500 fs (Figure 8C) with only weak variation of the coordination to Pt numbers and formation of absorbed propyne. Another C−H activation is observed at 25 ps (Figure 8C); however, no C−C breaking could be identified in our modeling. It is likely that coke formation involves a further reorganization mechanism between C3 fragments rather than direct C−C cleavage.

Evolution of the CVs in the case of SiO$_{2-700}$ supported Pt$_2$Ga nanoparticle is displayed in Figure 8D. The first C−H activation occurred as fast as for Pt (2 ps) in agreement with similar free energy of activation compared to pure Pt. However, due to the high distortion of the surface (Figure 8A), the formed intermediate is only monocoordinated to the Pt-surface and the C−H activation process is reversed around 3 ps to yield back propene (Figure 8D). Activation of the middle C−H group occurred at 5000 fs and a more stable Pt dicoordinated intermediate is produced. The system is then stuck for more than 20 ps: during this time neither the subsequent C−H activation leading to propyne nor C−C bond cleavage was observed, in contrast to the above-described case of Pt supported nanoparticles. The second activation finally takes place around 25 ps, but requires a significant reorganization of the nanoparticle to proceed (Figure 8A): during the 20 ps the number of PtGa bonds decreases while the number of Pt−Pt

bonds increases (Figure 8D). This reorganization allows a local increase of the Pt-concentration to stabilize Pt-tricoordinated propyne (Figure 8D). Such surface reorganization has also been proposed in the context of supported catalytically active liquid metal solutions (SCALMS).[20,110] The estimation of the activation energy for the second C−H activation of propene on PtGa is around 45 kcal mol^{-1} vs 15 kcal mol^{-1} in the case of Pt. This clearly indicates that coking is a highly disfavored process on Pt$_2$Ga compared to pure Pt in good agreement with the results obtained by static DFT calculations (see below).

As for PDH, we contrasted these results with static calculations on periodic surfaces (Figure 8B and Tables S16−S20). Starting from di-σ adsorbed propene a third Pt atom is required to promote the third C−H activation leading to the propenyl-platinum intermediate. A subsequent C−H activation step yields the most unsaturated intermediate, propyne, coordinated to three Pt atoms. As for the previous case the activation energy of each C−H activation step is directly related to the stability of the intermediates, and thus the activity difference between Pt and Pt$_2$Ga is always increasing with the dehydrogenation degree.

The last step is the scission of the C≡C triple bond to yield two surface alkylidyne Pt species moieties, Pt≡C−R (R = H, CH$_3$). This step requires the migration of one of these two fragments to a close-by Pt$_3$ cluster. While this is easy on Pt (111) ($\Delta G^{\ddagger}$ = +12.6 kcal mol^{-1}), it is extremely high in free energy (+53.7 kcal mol^{-1}) on Pt$_2$Ga (311) as the bis-ligated PtGa C-R intermediate is necessarily involved (Figure 8B). However, in contrast with the results from MTD calculations, subsequent C−H bond breaking (in the case R = H) is not favored.[38−40] This difference of reactivity is consistent with the significantly higher selectivity and resulting higher coking resistance of Pt$_2$Ga compared to Pt.

Overall, based on both MTD and static DFT results, the addition of Ga in Pt is expected to induce a strong decrease of the coke formation due to a combination of electronic (stabilization of the Pt d-orbitals, leading to a decrease of its electron donating ability) and steric effects (distortion and formation of isolated Pt$_3$ islands) of Ga. The two latter favor a higher selectivity and stability of the PtGa catalyst compared to Pt as experimentally observed.

5. CONCLUSION

In this study we used DFT calculations confronted with experimental data to refine the structure of highly active silica-supported PtGa nanoparticles for the PDH reaction. AIMD optimization of supported nanoparticles shows that, within the alloy, Pt atoms maximize their interaction with Ga, while Ga−Ga bond formation is disfavored. At the interface between the nanoparticle and the oxide support, both Pt^0 and Ga^0 interact with Si−O bonds; it is accompanied by additional Pt^0 interaction with remaining Ga^{III} Lewis acid sites. These nanoparticle−support interactions, described with molecular level precision, lead to a flattening of the nanoparticles and most likely play an important role for the stability of these PtGa PDH catalysts by preventing sintering. Additionally, these modeled structures explain and reconcile the earlier thought-to-be contradicting XAS and XPS data. We think that this approach, that confronts AIMD optimized structures with sets of experimental data, is a powerful methodology to refine the structure of complex systems, consisting of nanometric particles dispersed on (amorphous) supports, the detailed structure of which is not readily accessible via state-of-the-art spectroscopy/

electron microscopy. Besides structural information, AIMD also evidences the highly dynamic nature of the bimetallic nanoparticle surface compared to the monometallic Pt surface.

Regarding their formation, this study indicates that PtGa nanoparticles, prepared via SOMC from grafted Pt sites on Ga-doped silica treated under H_2, are formed in a stepwise way, first involving the fast formation of small Pt clusters/nanoparticles at low temperature from readily reducible isolated Pt^{II} sites as evidenced by XANES/EXAFS analysis. These Pt nanoparticles further react at higher temperatures with isolated Ga^{III} sites to generate the nanometric alloyed PtGa particles that interact with the silica surface and the residual Ga^{III} sites.

Finally, metadynamics simulations using realistic models for silica-supported nanoparticles as well as static DFT calculations on periodic surfaces also provide insight regarding the relation between the structures/dynamics of supported PtGa nanoparticles and their high performance toward PDH. First, PtGa alloying minimizes large Pt ensembles leading to Pt site isolation at the surface of the nanoparticles and increases the mobility of Pt atoms in the alloyed nanoparticles. This suggests transient and recurring formation of unsaturated Pt isolated sites that are highly active toward the first C−H activation steps. Second, site isolation of Pt atoms in the alloy disfavors coking through a combination of dilution, dynamic, and electronic effects. The adjunction of Ga to Pt decreases the affinity of Pt toward unsaturated hydrocarbon intermediates. Furthermore, since the formation of tri-Pt-coordinated propyne intermediates, a precursor for coke formation, would require an unfavorable partial PtGa dealloying to provide larger Pt ensembles, coke formation is prevented. The higher selectivity and stability of PtGa-based catalysts toward PDH can thus be related to the high energetic cost associated with such reorganization. Overall, this work supports that site isolation of Pt in highly dynamic PtGa alloyed nanoparticles and nanoparticle stabilization by a strong interaction with the support surface are key factors that explain the high catalytic performance in alkane dehydrogenation.

■ ASSOCIATED CONTENT

Supporting Information

The Supporting Information is available free of charge at https://pubs.acs.org/doi/10.1021/jacsau.1c00212.

> Experimental procedures, detailed computational procedures, optimize structures, and additional experimental data (XANES data, fittings, and TEM pictures) (PDF)
>
> Metadynamic movies (ZIP)

■ AUTHOR INFORMATION

Corresponding Authors

A. Comas-Vives − *Departament de Química, Universitat Autònoma de Barcelona, 08193 Cerdanyola del Vallès, Catalonia, Spain;* ● orcid.org/0000-0002-7002-1582; Email: aleix.comas@uab.cat

C. Copéret − *Department of Chemistry and Applied Biosciences, ETH Zürich, CH-8093 Zürich, Switzerland;* ● orcid.org/0000-0001-9660-3890; Email: ccoperet@ethz.ch

Authors

P.-A. Payard − *Department of Chemistry and Applied Biosciences, ETH Zürich, CH-8093 Zürich, Switzerland;* Present Address: P.-A.P.: Univ Lyon, Université Claude Bernard Lyon I, CNRS, INSA, CPE, UMR 5246, ICBMS, 1

rue Victor Grignard, F-69622 Villeurbanne cedex, France.; ● orcid.org/0000-0001-5661-6128

L. Rochlitz − *Department of Chemistry and Applied Biosciences, ETH Zürich, CH-8093 Zürich, Switzerland*

K. Searles − *Department of Chemistry and Applied Biosciences, ETH Zürich, CH-8093 Zürich, Switzerland;* Present Address: K.S.: University of Florida Department of Chemistry Gainesville Florida 32611−7200, USA.

L. Foppa − *Department of Chemistry and Applied Biosciences, ETH Zürich, CH-8093 Zürich, Switzerland;* Present Address: L.F.: Novel Materials Discovery Laboratory (NOMAD), Fritz-Haber-Institut der Max-Planck-Gesellschaft, 14195 Berlin, Germany.

B. Leuthold − *Department of Chemistry and Applied Biosciences, ETH Zürich, CH-8093 Zürich, Switzerland*

O. V. Safonova − *Paul Scherrer Institut, CH-5232 Villigen, Switzerland;* ● orcid.org/0000-0002-6772-1414

Complete contact information is available at: https://pubs.acs.org/10.1021/jacsau.1c00212

■ ACKNOWLEDGMENTS

■ REFERENCES

(1) Rodríguez-Vallejo, D. F.; Guillén-Gosálbez, G.; Chachuat, B. What Is the True Cost of Producing Propylene from Methanol? The Role of Externalities. *ACS Sustainable Chem. Eng.* **2020**, *8* (8), 3072−3081.

(2) Nawaz, Z. Light alkane dehydrogenation to light olefin technologies: a comprehensive review. *Rev. Chem. Eng.* **2015**, *31* (5), 413−436.

(3) Gallezot, P.; Leclercq, C.; Barbier, J.; Marecot, P. Location and structure of coke deposits on alumina-supported platinum catalysts by EELS associated with electron microscopy. *J. Catal.* **1989**, *116* (1), 164−170.

(4) Docherty, S. R.; Rochlitz, L.; Payard, P.-A.; Copéret, C. Heterogeneous alkane dehydrogenation catalysts investigated via a surface organometallic chemistry approach. *Chem. Soc. Rev.* **2021**, *50*, 5806−5822.

(5) Chen, S.; Chang, X.; Sun, G.; Zhang, T.; Xu, Y.; Wang, Y.; Pei, C.; Gong, J. Propane dehydrogenation: catalyst development, new chemistry, and emerging technologies. *Chem. Soc. Rev.* **2021**, *50* (5), 3315−3354.

(6) Han, Z.; Li, S.; Jiang, F.; Wang, T.; Ma, X.; Gong, J. Propane dehydrogenation over Pt−Cu bimetallic catalysts: the nature of coke deposition and the role of copper. *Nanoscale* **2014**, *6* (17), 10000−10008.

(7) Ma, Z.; Wu, Z.; Miller, J. T. Effect of Cu content on the bimetallic Pt−Cu catalysts for propane dehydrogenation. *Catal. Struct. React.* **2017**, *3* (1−2), 43−53.

(8) Veldurthi, S.; Shin, C.-H.; Joo, O.-S.; Jung, K.-D. Promotional effects of Cu on Pt/Al2O3 and Pd/Al2O3 catalysts during n-butane dehydrogenation. *Catal. Today* **2012**, *185* (1), 88−93.

(9) Yokoyama, C.; Bharadwaj, S. S.; Schmidt, L. D. Platinum-tin and platinum-copper catalysts for autothermal oxidative dehydrogenation of ethane to ethylene. *Catal. Lett.* **1996**, *38* (3), 181−188.

(10) Wu, J.; Mallikarjun Sharada, S.; Ho, C.; Hauser, A. W.; Head-Gordon, M.; Bell, A. T. Ethane and propane dehydrogenation over PtIr/Mg(Al)O. *Appl. Catal., A* **2015**, *506*, 25−32.

(11) Galvita, V.; Siddiqi, G.; Sun, P.; Bell, A. T. Ethane dehydrogenation on Pt/Mg(Al)O and PtSn/Mg(Al)O catalysts. *J. Catal.* **2010**, *271* (2), 209−219.

(12) Nawaz, Z.; Tang, X.; Wang, Y.; Wei, F. Parametric Characterization and Influence of Tin on the Performance of Pt−Sn/SAPO-34 Catalyst for Selective Propane Dehydrogenation to Propylene. *Ind. Eng. Chem. Res.* **2010**, *49* (3), 1274−1280.

(13) Zhang, Y.; Zhou, Y.; Qiu, A.; Wang, Y.; Xu, Y.; Wu, P. Propane dehydrogenation on PtSn/ZSM-5 catalyst: Effect of tin as a promoter. *Catal. Commun.* **2006**, *7* (11), 860−866.

(14) Vu, B. K.; Song, M. B.; Ahn, I. Y.; Suh, Y.-W.; Suh, D. J.; Kim, W.-I.; Koh, H.-L.; Choi, Y. G.; Shin, E. W. Pt−Sn alloy phases and coke mobility over Pt−Sn/Al2O3 and Pt−Sn/ZnAl2O4 catalysts for propane dehydrogenation. *Appl. Catal., A* **2011**, *400* (1), 25−33.

(15) Siddiqi, G.; Sun, P.; Galvita, V.; Bell, A. T. Catalyst performance of novel Pt/Mg(Ga)(Al)O catalysts for alkane dehydrogenation. *J. Catal.* **2010**, *274* (2), 200−206.

(16) Sun, P.; Siddiqi, G.; Chi, M.; Bell, A. T. Synthesis and characterization of a new catalyst Pt/Mg(Ga)(Al)O for alkane dehydrogenation. *J. Catal.* **2010**, *274* (2), 192−199.

(17) Sattler, J. J. H. B.; Gonzalez-Jimenez, I. D.; Luo, L.; Stears, B. A.; Malek, A.; Barton, D. G.; Kilos, B. A.; Kaminsky, M. P.; Verhoeven, T. W. G. M.; Koers, E. J.; Baldus, M.; Weckhuysen, B. M. Platinum-Promoted Ga/Al2O3 as Highly Active, Selective, and Stable Catalyst for the Dehydrogenation of Propane. *Angew. Chem., Int. Ed.* **2014**, *53* (35), 9251−9256.

(18) Searles, K.; Chan, K. W.; Mendes Burak, J. A.; Zemlyanov, D.; Safonova, O.; Copéret, C. Highly Productive Propane Dehydrogenation Catalyst Using Silica-Supported Ga−Pt Nanoparticles Generated from Single-Sites. *J. Am. Chem. Soc.* **2018**, *140* (37), 11674−11679.

(19) Im, J.; Choi, M. Physicochemical Stabilization of Pt against Sintering for a Dehydrogenation Catalyst with High Activity, Selectivity, and Durability. *ACS Catal.* **2016**, *6* (5), 2819−2826.

(20) Bauer, T.; Maisel, S.; Blaumeiser, D.; Vecchietti, J.; Taccardi, N.; Wasserscheid, P.; Bonivardi, A.; Görling, A.; Libuda, J. Operando DRIFTS and DFT Study of Propane Dehydrogenation over Solid- and Liquid-Supported GaxPty Catalysts. *ACS Catal.* **2019**, *9* (4), 2842−2853.

(21) Jablonski, E. L.; Castro, A. A.; Scelza, O. A.; de Miguel, S. R. Effect of Ga addition to Pt/Al2O3 on the activity, selectivity and deactivation in the propane dehydrogenation. *Appl. Catal., A* **1999**, *183* (1), 189−198.

(22) Iezzi, R.; Bartolini, A.; Buonomo, F. Process for Preparing Light Olefins by Dehydrogenation of the Corresponding Paraffins. US7235706B2, 2007.

(23) Lou, L.; Rosenfeld, D.; Malek, A. M. Reconstituted Dehydrogenation Catalyst Showing Slowed Activity Loss When Compared With Fresh Catalyst. WO2013/126210Al, 2013.

(24) Wang, T.; Jiang, F.; Liu, G.; Zeng, L.; Zhao, Z.-j.; Gong, J. Effects of Ga doping on Pt/CeO2-Al2O3 catalysts for propane dehydrogenation. *AIChE J.* **2016**, *62* (12), 4365−4376.

(25) Nakaya, Y.; Hirayama, J.; Yamazoe, S.; Shimizu, K.-i.; Furukawa, S. Single-atom Pt in intermetallics as an ultrastable and selective catalyst for propane dehydrogenation. *Nature Commun.* **2020**, *11* (1), 2838.

(26) Tolek, W.; Suriye, K.; Praserthdam, P.; Panpranot, J. Enhanced Stability and Propene Yield in Propane Dehydrogenation on PtIn/Mg(Al)O Catalysts with Various In Loadings. *Top. Catal.* **2018**, *61* (15), 1624−1632.

(27) Shen, L.-L.; Xia, K.; Lang, W.-Z.; Chu, L.-F.; Yan, X.; Guo, Y.-J. The effects of calcination temperature of support on PtIn/Mg(Al)O

(28) Xia, K.; Lang, W.-Z.; Li, P.-P.; Yan, X.; Guo, Y.-J. The properties and catalytic performance of PtIn/Mg(Al)O catalysts for the propane dehydrogenation reaction: Effects of pH value in preparing Mg(Al)O supports by the co-precipitation method. *J. Catal.* **2016**, *338*, 104−114.

(29) Camacho-Bunquin, J.; Ferrandon, M. S.; Sohn, H.; Kropf, A. J.; Yang, C.; Wen, J.; Hackler, R. A.; Liu, C.; Celik, G.; Marshall, C. L.; Stair, P. C.; Delferro, M. Atomically Precise Strategy to a PtZn Alloy Nanocluster Catalyst for the Deep Dehydrogenation of n-Butane to 1,3-Butadiene. *ACS Catal.* **2018**, *8* (11), 10058−10063.

(30) Chen, C.; Sun, M.; Hu, Z.; Ren, J.; Zhang, S.; Yuan, Z.-Y. New insight into the enhanced catalytic performance of ZnPt/HZSM-5 catalysts for direct dehydrogenation of propane to propylene. *Catal. Sci. Technol.* **2019**, *9* (8), 1979−1988.

(31) Rochlitz, L.; Searles, K.; Alfke, J.; Zemlyanov, D.; Safonova, O. V.; Copéret, C. Silica-supported, narrowly distributed, subnanometric Pt−Zn particles from single sites with high propane dehydrogenation performance. *Chem. Sci.* **2020**, *11* (6), 1549−1555.

(32) Cybulskis, V. J.; Bukowski, B. C.; Tseng, H.-T.; Gallagher, J. R.; Wu, Z.; Wegener, E.; Kropf, A. J.; Ravel, B.; Ribeiro, F. H.; Greeley, J.; Miller, J. T. Zinc Promotion of Platinum for Catalytic Light Alkane Dehydrogenation: Insights into Geometric and Electronic Effects. *ACS Catal.* **2017**, *7* (6), 4173−4181.

(33) Yu, C.; Xu, H.; Ge, Q.; Li, W. Properties of the metallic phase of zinc-doped platinum catalysts for propane dehydrogenation. *J. Mol. Catal. A: Chem.* **2007**, *266* (1), 80−87.

(34) Gao, J.; Zhao, H.; Yang, X.; Koel, B. E.; Podkolzin, S. G. Controlling Acetylene Adsorption and Reactions on Pt−Sn Catalytic Surfaces. *ACS Catal.* **2013**, *3* (6), 1149−1153.

(35) Vila, F. D.; Rehr, J. J.; Kelly, S. D.; Bare, S. R. Operando Effects on the Structure and Dynamics of PtnSnm/γ-Al2O3 from Ab Initio Molecular Dynamics and X-ray Absorption Spectra. *J. Phys. Chem. C* **2013**, *117* (24), 12446−12457.

(36) Nykänen, L.; Honkala, K. Selectivity in Propene Dehydrogenation on Pt and Pt3Sn Surfaces from First Principles. *ACS Catal.* **2013**, *3* (12), 3026−3030.

(37) Hauser, A. W.; Gomes, J.; Bajdich, M.; Head-Gordon, M.; Bell, A. T. Subnanometer-sized Pt/Sn alloy cluster catalysts for the dehydrogenation of linear alkanes. *Phys. Chem. Chem. Phys.* **2013**, *15* (47), 20727−20734.

(38) Sui, Z.-J.; Zhu, Y.-A.; Li, P.; Zhou, X.-G.; Chen, D., Chapter Two - Kinetics of Catalytic Dehydrogenation of Propane over Pt-Based Catalysts. In *Advances in Chemical Engineering*; Marin, G. B., Ed.; Academic Press: 2014; Vol. 44, pp 61−125.

(39) Yang, M.-L.; Zhu, Y.-A.; Fan, C.; Sui, Z.-J.; Chen, D.; Zhou, X.-G. DFT study of propane dehydrogenation on Pt catalyst: effects of step sites. *Phys. Chem. Chem. Phys.* **2011**, *13* (8), 3257−3267.

(40) Yang, M.-L.; Zhu, Y.-A.; Fan, C.; Sui, Z.-J.; Chen, D.; Zhou, X.-G. Density functional study of the chemisorption of C1, C2 and C3 intermediates in propane dissociation on Pt(111). *J. Mol. Catal. A: Chem.* **2010**, *321* (1), 42−49.

(41) Wang, Y.; Hu, P.; Yang, J.; Zhu, Y.-A.; Chen, D. C−H bond activation in light alkanes: a theoretical perspective. *Chem. Soc. Rev.* **2021**, *50* (7), 4299−4358.

(42) Völter, J.; Lietz, G.; Uhlemann, M.; Hermann, M. Conversion of cyclohexane and n-heptane on Pt-PbAl2O3 and Pt-SnAl2O3 bimetallic catalysts. *J. Catal.* **1981**, *68* (1), 42−50.

(43) Lieske, H.; Sárkány, A.; Völter, J. Hydrocarbon adsorption and coke formation on Pt/Al2O3 and Pt-Sn/Al2O3 catalysts. *Appl. Catal.* **1987**, *30* (1), 69−80.

(44) Liwu, L.; Tao, Z.; Jingling, Z.; Zhusheng, X. Dynamic process of carbon deposition on Pt and Pt−Sn catalysts for alkane dehydrogenation. *Appl. Catal.* **1990**, *67* (1), 11−23.

(45) Larsson, M.; Hultén, M.; Blekkan, E. A.; Andersson, B. The Effect of Reaction Conditions and Time on Stream on the Coke Formed during Propane Dehydrogenation. *J. Catal.* **1996**, *164* (1), 44−53.

(46) Li, Q.; Sui, Z.; Zhou, X.; Zhu, Y.; Zhou, J.; Chen, D. Coke Formation on Pt−Sn/Al2O3 Catalyst in Propane Dehydrogenation:

Coke Characterization and Kinetic Study. *Top. Catal.* **2011**, *54* (13), 888.

(47) (a) Pretz, M.; Fish, B.; Luo, L.; Stears, B. Shaping the future of on-purpose propylene production. *Hydrocarb. Process* **2017**, 4. (b) Pretz, M. T.; Domke, S. B.; Castor, W. M.; Hamper, S. J. Process for the preparation of dehydrogenated hydrocarbon compounds. EP2495228B1, 2012. (c) Pretz, M. T.; Stewart, M. W. Catalytic dehydrogenation process.US9725382B2, 2014. (d) Pretz, M. T.; Luo, L.; Domke, S.; Clark, H. W.; Pierce, R. A.; Malek, A. M.; Stewart, M. W.; Stears, B. A.; Schweizer, A. E.; Capone, G.; Coffey, D. P.; Mbaraka, I. K. Reactivating propane dehydrogenation catalyst. US10065905B2, 2018.

(48) Guisnet, M.; Lukyanov, D.; Hattori, H.; Misono, M.; Ono, Y. 4.2 Aromatization of Short Chain Alkanes on Ga MFI Catalysts. *Stud. Surf. Sci. Catal.* **1994**, *90*, 367−378.

(49) Nakagawa, K.; Okamura, M.; Ikenaga, N.; Suzuki, T.; Nakagawa, K.; Okamura, M.; Suzuki, T.; Kobayashi, T.; Kobayashi, T. Dehydrogenation of ethane over gallium oxide in the presence of carbon dioxide. *Chem. Commun.* **1998**, 1025−1026.

(50) Zheng, B.; Hua, W.; Yue, Y.; Gao, Z. Dehydrogenation of propane to propene over different polymorphs of gallium oxide. *J. Catal.* **2005**, *232* (1), 143−151.

(51) Searles, K.; Siddiqi, G.; Safonova, O. V.; Copéret, C. Silica-supported isolated gallium sites as highly active, selective and stable propane dehydrogenation catalysts. *Chem. Sci.* **2017**, *8* (4), 2661−2666.

(52) Kazansky, V. B.; Subbotina, I. R.; Pronin, A. A.; Schlögl, R.; Jentoft, F. C. Unusual Infrared Spectrum of Ethane Adsorbed by Gallium Oxide. *J. Phys. Chem. B* **2006**, *110* (15), 7975−7978.

(53) Pereira, M. S.; Chaer Nascimento, M. A. Theoretical Study on the Dehydrogenation Reaction of Alkanes Catalyzed by Zeolites Containing Nonframework Gallium Species. *J. Phys. Chem. B* **2006**, *110* (7), 3231−3238.

(54) Pidko, E. A.; Hensen, E. J. M.; van Santen, R. A. Dehydrogenation of Light Alkanes over Isolated Gallyl Ions in Ga/ZSM-5 Zeolites. *J. Phys. Chem. C* **2007**, *111* (35), 13068−13075.

(55) Liu, Y.; Li, Z. H.; Lu, J.; Fan, K.-N. Periodic Density Functional Theory Study of Propane Dehydrogenation over Perfect Ga2O3 (100) Surface. *J. Phys. Chem. C* **2008**, *112* (51), 20382−20392.

(56) Gabrienko, A. A.; Arzumanov, S. S.; Toktarev, A. V.; Stepanov, A. G. Metal-alkyl species are formed on interaction of small alkanes with gallium oxide: Evidence from solid-state NMR. *Chem. Phys. Lett.* **2010**, *496* (1), 148−151.

(57) Only trend calculation to aiming at finding out general trends about PtX alloy selectivity against coking were calculated in the several studies: (a) Hook, A.; Celik, F. E. Predicting Selectivity for Ethane Dehydrogenation and Coke Formation Pathways over Model Pt−M Surface Alloys with ab Initio and Scaling Methods. *J. Phys. Chem. C* **2017**, *121* (33), 17882−17892. (b) Zha, S.; Sun, G.; Wu, T.; Zhao, J.; Zhao, Z.-J.; Gong, J. Identification of Pt-based catalysts for propane dehydrogenation via a probability analysis. *Chem. Sci.* **2018**, *9* (16), 3925−3931. (c) Sun, G.; Zhao, Z.-J.; Mu, R.; Zha, S.; Li, L.; Chen, S.; Zang, K.; Luo, J.; Li, Z.; Purdy, S. C.; Kropf, A. J.; Miller, J. T.; Zeng, L.; Gong, J. Breaking the scaling relationship via thermally stable Pt/Cu single atom alloys for catalytic dehydrogenation. *Nat. Commun.* **2018**, *9* (1), 4454.

(58) Stalzer, M. M.; Delferro, M.; Marks, T. J. Supported Single-Site Organometallic Catalysts for the Synthesis of High-Performance Polyolefins. *Catal. Lett.* **2015**, *145* (1), 3−14.

(59) Pelletier, J. D. A.; Basset, J.-M. Catalysis by Design: Well-Defined Single-Site Heterogeneous Catalysts. *Acc. Chem. Res.* **2016**, *49* (4), 664−677.

(60) Copéret, C.; Allouche, F.; Chan, K. W.; Conley, M. P.; Delley, M. F.; Fedorov, A.; Moroz, I. B.; Mougel, V.; Pucino, M.; Searles, K.; Yamamoto, K.; Zhizhko, P. A. Bridging the Gap between Industrial and Well-Defined Supported Catalysts. *Angew. Chem., Int. Ed.* **2018**, *57* (22), 6398−6440.

(61) Copéret, C.; Comas-Vives, A.; Conley, M. P.; Estes, D. P.; Fedorov, A.; Mougel, V.; Nagae, H.; Núñez-Zarur, F.; Zhizhko, P. A. Surface Organometallic and Coordination Chemistry toward Single-Site Heterogeneous Catalysts: Strategies, Methods, Structures, and Activities. *Chem. Rev.* **2016**, *116* (2), 323−421.

(62) Copéret, C.; Chabanas, M.; Petroff Saint-Arroman, R.; Basset, J.-M. Homogeneous and Heterogeneous Catalysis: Bridging the Gap through Surface Organometallic Chemistry. *Angew. Chem., Int. Ed.* **2003**, *42* (2), 156−181.

(63) Pham, H. N.; Sattler, J. J. H. B.; Weckhuysen, B. M.; Datye, A. K. Role of Sn in the Regeneration of Pt/γ-Al2O3 Light Alkane Dehydrogenation Catalysts. *ACS Catal.* **2016**, *6* (4), 2257−2264.

(64) Wu, J.; Peng, Z.; Bell, A. T. Effects of composition and metal particle size on ethane dehydrogenation over PtxSn100−x/Mg(Al)O (70⩽x⩽100). *J. Catal.* **2014**, *311*, 161−168.

(65) Marx, D.; Hutter, J. *Ab Initio Molecular Dynamics: Basic Theory and Advanced Methods*; Cambridge University Press: Cambridge, 2009. DOI: 10.1017/CBO9780511609633.

(66) Marx, D.; Hutter, J., Ab initio molecular dynamics: Theory and implementation. In *Modern methods and algorithms of quantum chemistry*; NIC-Directors: Jülich, Germany, 2000; Vol. 3, p 329.

(67) Ensing, B.; De Vivo, M.; Liu, Z.; Moore, P.; Klein, M. L. Metadynamics as a Tool for Exploring Free Energy Landscapes of Chemical Reactions. *Acc. Chem. Res.* **2006**, *39* (2), 73−81.

(68) Iannuzzi, M.; Laio, A.; Parrinello, M. Efficient Exploration of Reactive Potential Energy Surfaces Using Car-Parrinello Molecular Dynamics. *Phys. Rev. Lett.* **2003**, *90* (23), 238302.

(69) Laio, A.; Parrinello, M. Escaping free-energy minima. *Proc. Natl. Acad. Sci. U. S. A.* **2002**, *99* (20), 12562.

(70) Barducci, A.; Bonomi, M.; Parrinello, M. Metadynamics. *Wiley Interdiscip. Rev.: Comput. Mol. Sci.* **2011**, *1* (5), 826−843.

(71) Kresse, G.; Hafner, J. Ab initio molecular dynamics for liquid metals. *Phys. Rev. B: Condens. Matter Mater. Phys.* **1993**, *47* (1), 558−561.

(72) Kresse, G.; Hafner, J. Ab initio molecular-dynamics simulation of the liquid-metal–amorphous-semiconductor transition in germanium. *Phys. Rev. B: Condens. Matter Mater. Phys.* **1994**, *49* (20), 14251−14269.

(73) Kresse, G.; Furthmüller, J. Efficiency of ab-initio total energy calculations for metals and semiconductors using a plane-wave basis set. *Comput. Mater. Sci.* **1996**, *6* (1), 15−50.

(74) Kresse, G.; Furthmüller, J. Efficient iterative schemes for ab initio total-energy calculations using a plane-wave basis set. *Phys. Rev. B: Condens. Matter Mater. Phys.* **1996**, *54* (16), 11169−11186.

(75) Perdew, J. P.; Burke, K.; Ernzerhof, M. Generalized Gradient Approximation Made Simple. *Phys. Rev. Lett.* **1996**, *77* (18), 3865−3868.

(76) Grimme, S.; Ehrlich, S.; Goerigk, L. Effect of the damping function in dispersion corrected density functional theory. *J. Comput. Chem.* **2011**, *32* (7), 1456−1465.

(77) Grimme, S.; Antony, J.; Ehrlich, S.; Krieg, H. A consistent and accurate ab initio parametrization of density functional dispersion correction (DFT-D) for the 94 elements H-Pu. *J. Chem. Phys.* **2010**, *132* (15), 154104.

(78) Zhang, Y.; Yang, W. Comment on "Generalized Gradient Approximation Made Simple". *Phys. Rev. Lett.* **1998**, *80* (4), 890−890.

(79) Blöchl, P. E. Projector augmented-wave method. *Phys. Rev. B: Condens. Matter Mater. Phys.* **1994**, *50* (24), 17953−17979.

(80) Kresse, G.; Joubert, D. From ultrasoft pseudopotentials to the projector augmented-wave method. *Phys. Rev. B: Condens. Matter Mater. Phys.* **1999**, *59* (3), 1758−1775.

(81) Nykänen, L.; Honkala, K. Density Functional Theory Study on Propane and Propene Adsorption on Pt(111) and PtSn Alloy Surfaces. *J. Phys. Chem. C* **2011**, *115* (19), 9578−9586.

(82) Bengtsson, L. Dipole correction for surface supercell calculations. *Phys. Rev. B: Condens. Matter Mater. Phys.* **1999**, *59* (19), 12301−12304.

(83) Gautier, S.; Steinmann, S. N.; Michel, C.; Fleurat-Lessard, P.; Sautet, P. Molecular adsorption at Pt(111). How accurate are DFT functionals? *Phys. Chem. Chem. Phys.* **2015**, *17* (43), 28921−28930.

(84) Mager-Maury, C.; Chizallet, C.; Sautet, P.; Raybaud, P. Platinum Nanoclusters Stabilized on γ-Alumina by Chlorine Used As a Capping

Surface Ligand: A Density Functional Theory Study. *ACS Catal.* **2012**, *2* (7), 1346−1357.

(85) Sun, G.; Alexandrova, A. N.; Sautet, P. Structural Rearrangements of Subnanometer Cu Oxide Clusters Govern Catalytic Oxidation. *ACS Catal.* **2020**, *10*, 5309−5317.

(86) Gorczyca, A.; Raybaud, P.; Moizan, V.; Joly, Y.; Chizallet, C. Atomistic Models for Highly-Dispersed PtSn/γ-Al2O3 Catalysts: Ductility and Dilution Affect the Affinity for Hydrogen. *ChemCatChem* **2019**, *11* (16), 3941−3951.

(87) Wang, Y.; Xiang, B.; Yang, H.-Q.; Hu, C.-W. Density Functional Theory Study on the Nucleation and Growth of Ptn Clusters on γ-Al2O3 (001) Surface. *ACS Omega* **2017**, *2* (7), 3250−3259.

(88) Zhai, H.; Alexandrova, A. N. Correction to "Local Fluxionality of Surface-Deposited Cluster Catalysts: The Case of Pt7 on Al2O3. *J. Phys. Chem. Lett.* **2018**, *9* (20), 6011−6011.

(89) Zhai, H.; Alexandrova, A. N. Local Fluxionality of Surface-Deposited Cluster Catalysts: The Case of Pt7 on Al2O3. *J. Phys. Chem. Lett.* **2018**, *9* (7), 1696−1702.

(90) Silaghi, M.-C.; Comas-Vives, A.; Copéret, C. CO2 Activation on Ni/γ−Al2O3 Catalysts by First-Principles Calculations: From Ideal Surfaces to Supported Nanoparticles. *ACS Catal.* **2016**, *6* (7), 4501−4505.

(91) Larmier, K.; Liao, W.-C.; Tada, S.; Lam, E.; Verel, R.; Bansode, A.; Urakawa, A.; Comas-Vives, A.; Copéret, C. CO2-to-Methanol Hydrogenation on Zirconia-Supported Copper Nanoparticles: Reaction Intermediates and the Role of the Metal−Support Interface. *Angew. Chem., Int. Ed.* **2017**, *56* (9), 2318−2323.

(92) Lam, E.; Corral-Pérez, J. J.; Larmier, K.; Noh, G.; Wolf, P.; Comas-Vives, A.; Urakawa, A.; Copéret, C. CO2 Hydrogenation on Cu/Al2O3: Role of the Metal/Support Interface in Driving Activity and Selectivity of a Bifunctional Catalyst. *Angew. Chem., Int. Ed.* **2019**, *58* (39), 13989−13996.

(93) VandeVondele, J.; Krack, M.; Mohamed, F.; Parrinello, M.; Chassaing, T.; Hutter, J. Quickstep: Fast and accurate density functional calculations using a mixed Gaussian and plane waves approach. *Comput. Phys. Commun.* **2005**, *167* (2), 103−128.

(94) Hutter, J.; Iannuzzi, M.; Schiffmann, F.; VandeVondele, J. cp2k: atomistic simulations of condensed matter systems. *WIREs Comput. Mol. Sci.* **2014**, *4* (1), 15−25.

(95) Lippert, B. G.; Parrinello, J. H.; Michele. A hybrid Gaussian and plane wave density functional scheme. *Mol. Phys.* **1997**, *92* (3), 477−488.

(96) Lippert, G.; Hutter, J.; Parrinello, M. The Gaussian and augmented-plane-wave density functional method for ab initio molecular dynamics simulations. *Theor. Chem. Acc.* **1999**, *103* (2), 124−140.

(97) VandeVondele, J.; Hutter, J. Gaussian basis sets for accurate calculations on molecular systems in gas and condensed phases. *J. Chem. Phys.* **2007**, *127* (11), 114105.

(98) Goedecker, S.; Teter, M.; Hutter, J. Separable dual-space Gaussian pseudopotentials. *Phys. Rev. B: Condens. Matter Mater. Phys.* **1996**, *54* (3), 1703−1710.

(99) Ruddy, D. A.; Jarupatrakorn, J.; Rioux, R. M.; Miller, J. T.; McMurdo, M. J.; McBee, J. L.; Tupper, K. A.; Tilley, T. D. Site-Isolated Pt-SBA15 Materials from Tris(tert-butoxy)siloxy Complexes of Pt(II) and Pt(IV). *Chem. Mater.* **2008**, *20* (20), 6517−6527.

(100) Müller, O.; Stötzel, J.; Lützenkirchen-Hecht, D.; Frahm, R. Gridded Ionization Chambers for Time Resolved X-Ray Absorption Spectroscopy. *J. Phys.: Conf. Ser.* **2013**, *425* (9), 092010.

(101) Ravel, B.; Newville, M. ATHENA, ARTEMIS, HEPHAESTUS: data analysis for X-ray absorption spectroscopy using IFEFFIT. *J. Synchrotron Radiat.* **2005**, *12* (4), 537−541.

(102) Comas-Vives, A. Amorphous SiO2 surface models: energetics of the dehydroxylation process, strain, ab initio atomistic thermodynamics and IR spectroscopic signatures. *Phys. Chem. Chem. Phys.* **2016**, *18* (10), 7475−7482.

(103) Praveen, C. S.; Borosy, A. P.; Copéret, C.; Comas-Vives, A. Strain in Silica-Supported Ga(III) Sites: Neither Too Much nor Too Little for Propane Dehydrogenation Catalytic Activity. *Inorg. Chem.* **2021**, *60* (10), 6865−6874.

(104) Laurent, P.; Veyre, L.; Thieuleux, C.; Donet, S.; Copéret, C. From well-defined Pt(ii) surface species to the controlled growth of silica supported Pt nanoparticles. *Dalton Trans.* **2013**, *42* (1), 238−248.

(105) Filez, M.; Redekop, E. A.; Galvita, V. V.; Poelman, H.; Meledina, M.; Turner, S.; Van Tendeloo, G.; Bell, A. T.; Marin, G. B. The role of hydrogen during Pt−Ga nanocatalyst formation. *Phys. Chem. Chem. Phys.* **2016**, *18* (4), 3234−3243.

(106) Danilina, N.; Payrer, E. L.; Troussard, E.; van Bokhoven, J. A. Selective Production of 2-Phenylhexane from Benzene and n-Hexane Over Pt- and Ga-Modified Zeolites. *Catal. Lett.* **2011**, *141* (3), 391−399.

(107) Demuth, J. E.; Ibach, H.; Lehwald, S. CH Vibration Softening and the Dehydrogenation of Hydrocarbon Molecules on Ni(111) and Pt(111). *Phys. Rev. Lett.* **1978**, *40* (15), 1044−1047.

(108) Hoffmann, F. M.; Upton, T. H. Carbon-hydrogen (CH)-metal interactions of adsorbed cyclic hydrocarbons. *J. Phys. Chem.* **1984**, *88* (25), 6209−6212.

(109) McMaster, M. C.; Arumainayagam, C. R.; Madix, R. J. Molecular propane adsorption dynamics on Pt(111). *Chem. Phys.* **1993**, *177* (2), 461−472.

(110) Kettner, M.; Maisel, S.; Stumm, C.; Schwarz, M.; Schuschke, C.; Görling, A.; Libuda, J. Pd-Ga model SCALMS: Characterization and stability of Pd single atom sites. *J. Catal.* **2019**, *369*, 33−46.

(111) The PLUMED consortium. Promoting transparency and reproducibility in enhanced molecular simulations. *Nat. Methods* **2019**, *16* (8), 670−673.

(112) Tribello, G. A.; Bonomi, M.; Branduardi, D.; Camilloni, C.; Bussi, G. PLUMED 2: New feathers for an old bird. *Comput. Phys. Commun.* **2014**, *185* (2), 604−613.